Science Advances
AAAS

advances.sciencemag.org/cgi/content/full/6/48/eabd1387/DC1

Supplementary Materials for

Redox state of Earth's magma ocean and its Venus-like early atmosphere

Paolo A. Sossi*, Antony D. Burnham, James Badro, Antonio Lanzirotti, Matt Newville, Hugh St.C. O'Neill

*Corresponding author. Email: paolo.sossi@erdw.ethz.ch

Published 25 November 2020, *Sci. Adv.* **6**, eabd1387 (2020)
DOI: 10.1126/sciadv.abd1387

This PDF file includes:

Supplementary Text

1. Temperature profiles and summary of laser levitation experiments

Summary of experimental conditions

Table S1. Conditions (temperature, run time, gas mixtures) of synthesis of peridotite glasses by aerodynamic laser levitation.

Sample	Temperature (°C)	Run time (s)	Ar (%)	CO_2 (%)	H_2 (%)	logfO_2	Gas Mixture
Per-fO_2 (1)	1900±21	30				0.00	O_2
Per-fO_2 (2)	1893±40	40	92	8		-2.49	CO_2
Per-fO_2 (3)	1861±29	32	92	7.92	0.08	-2.53	$99CO_2$:$1H_2$
Per-fO_2 (6)	1878±23	25	92	7.84	0.16	-2.58	$98CO_2$:$2H_2$
Per-TS1	1851±13	10	92	7.6	0.4	-2.72	$95CO_2$:$5H_2$
Per-fO_2 (7)	1866±13	27	92	7.6	0.4	-2.72	$95CO_2$:$5H_2$
Per-TS2	1875±41	120	92	7.6	0.4	-2.72	$95CO_2$:$5H_2$
Per-fO_2 (8)	1924±13	31	92	7.2	0.8	-3.00	$90CO_2$:$10H_2$
Per-fO_2 (9)	1902±15	30	92	6	2	-3.92	$75CO_2$:$25H_2$
Per-fO_2 (10)	1900±21	30	92	4	4	-5.32	$50CO_2$:$50H_2$
Per-fO_2 (11)	1896±16	28	92	2	6	-6.74	$25CO_2$:$75H_2$
Per-fO_2 (12)	1839±17	33	92	0.8	7.2	-7.86	$10CO_2$:$90H_2$

Recorded temperature-time traces of experiments

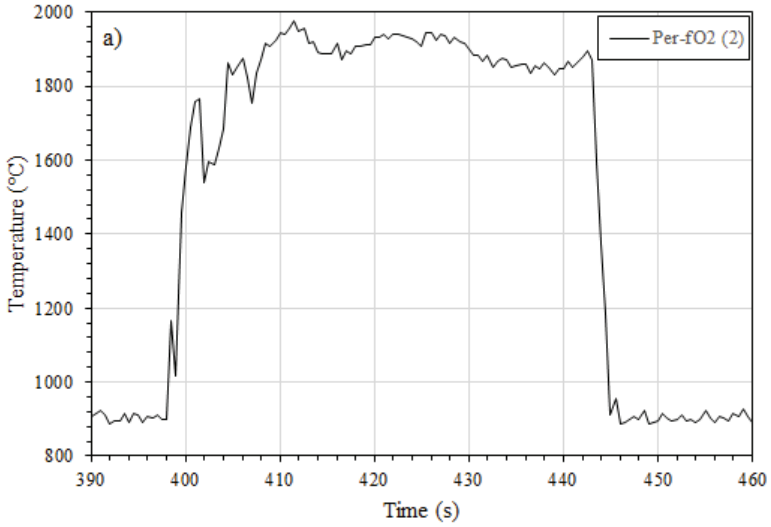

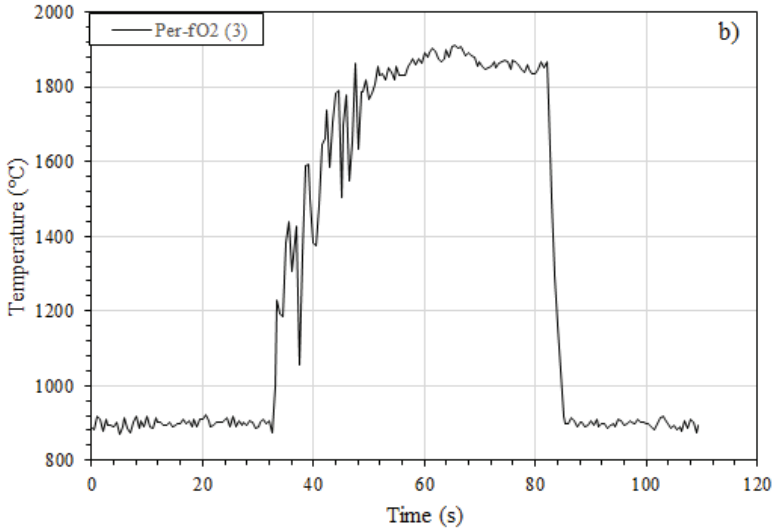

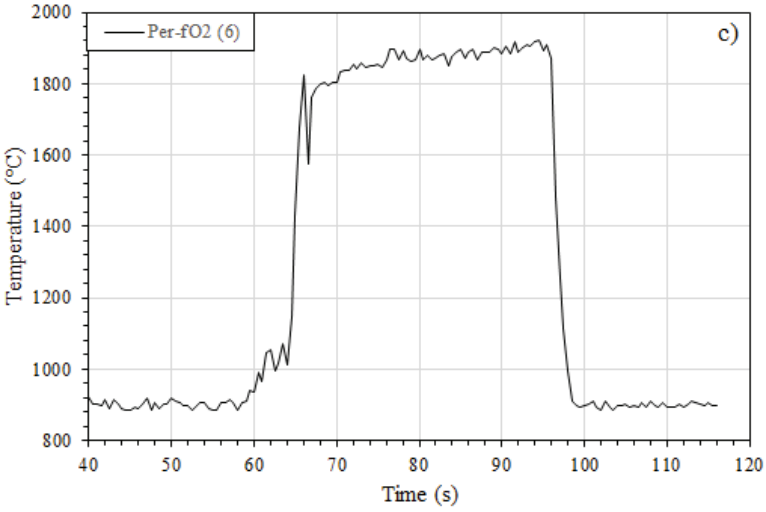

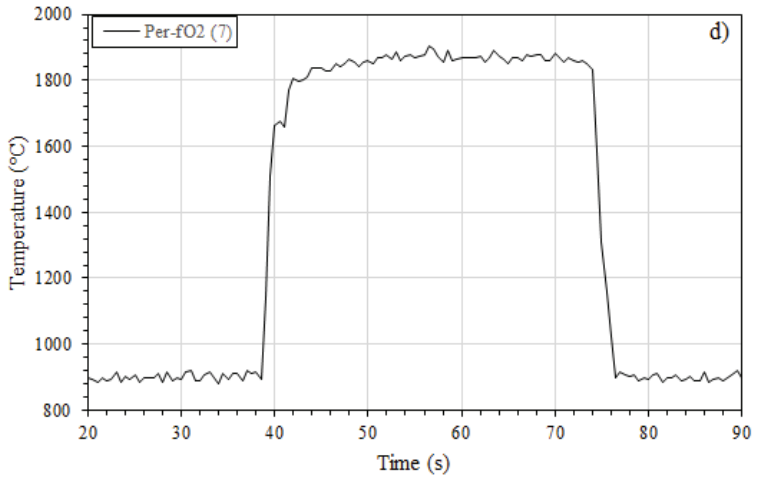
Per-fO2 (7)
d)
Temperature (°C)
Time (s)

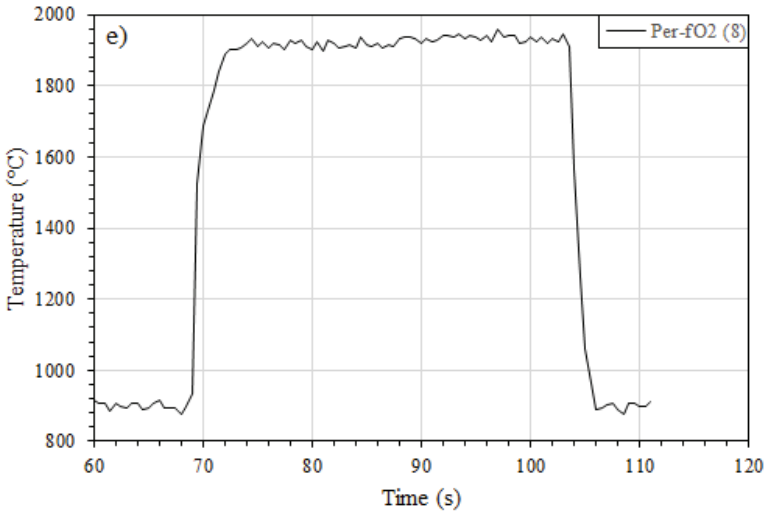
e)
Per-fO2 (8)
Temperature (°C)
Time (s)

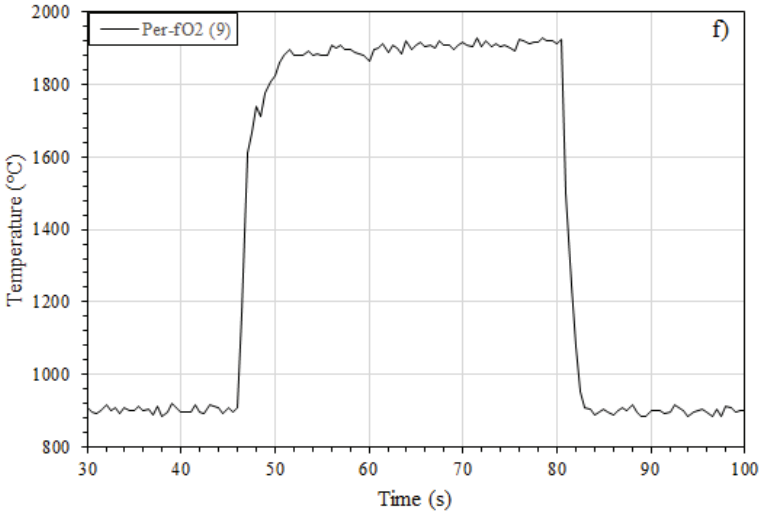
Per-fO2 (9)
f)
Temperature (°C)
Time (s)

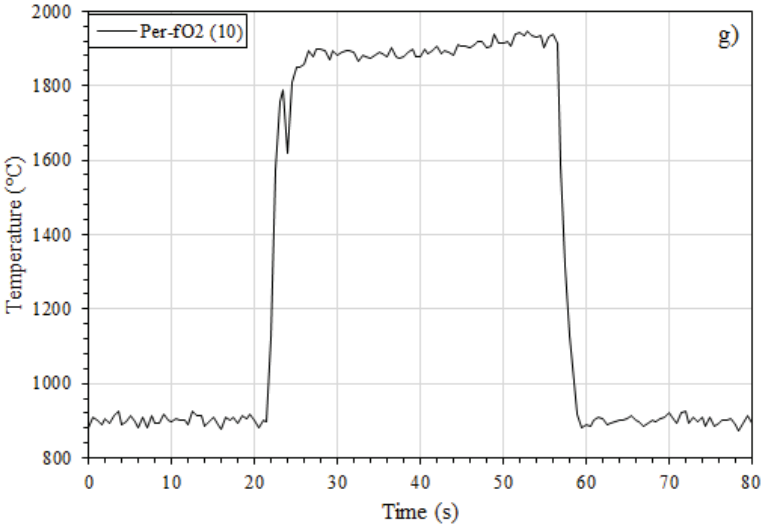
Per-fO2 (10)
g)
Temperature (°C)
Time (s)

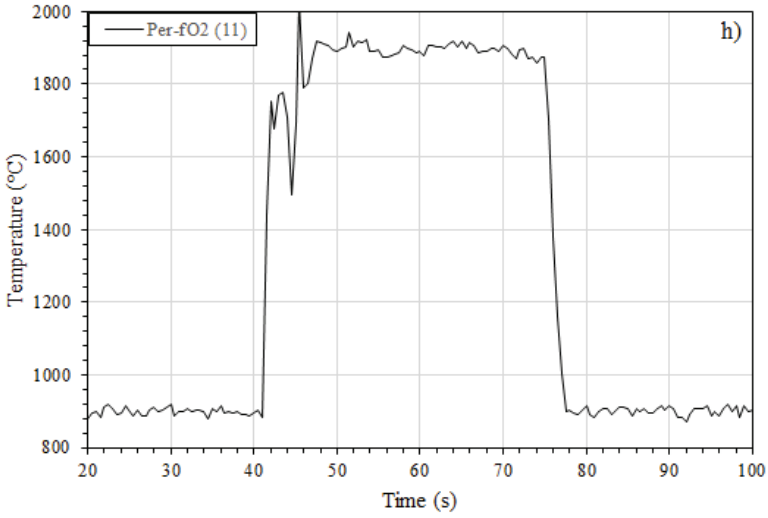
Per-fO2 (11)
h)
Temperature (°C)
Time (s)

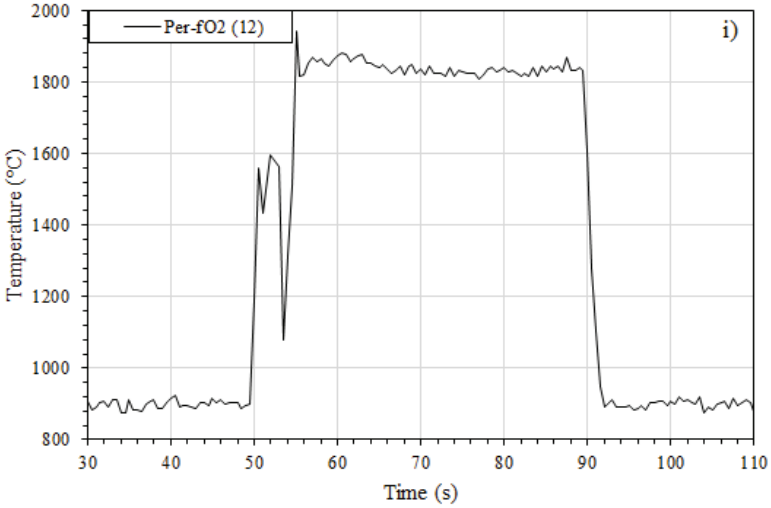
Per-fO2 (12)
i)
Temperature (°C)
Time (s)

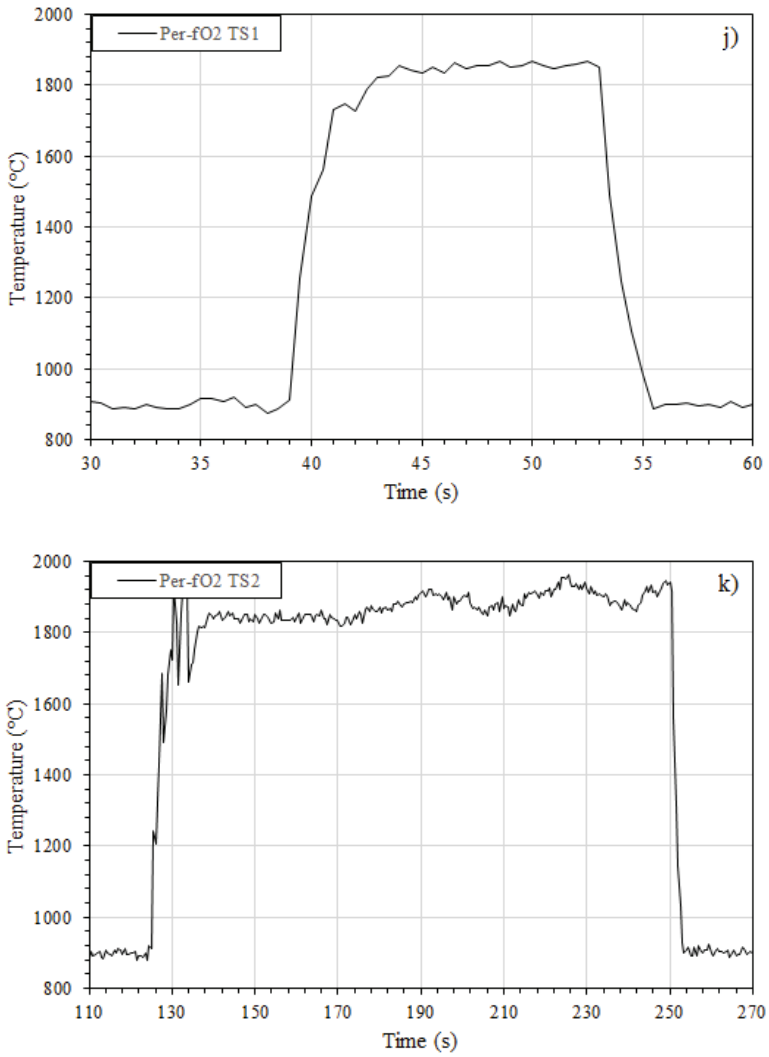

Fig. S1. a) to k) Temperature-time profiles of experimental glasses. Temperature of the melt bead during aerodynamic laser levitation experiments recorded *in-situ* by optical pyrometry. Sample name is given on the graph.

The temperature fluctuations observed at the commencement of the heating procedure (particularly in samples Per-fO_2 (2), (3), (12) and TS2) pertain to the instability of the sphere in the gas flow stream. The glass beads may randomly oscillate in the stream prior to entering a stable, aerodynamically levitated state, at which point the temperature control is precise to within ±15 °C (Table S1). The run time was calculated over the plateau for which heating was isothermal. The temperature uncertainty quoted in the main text (±50 °C) represents the temperature variability among the samples synthesised, rather than the inherent run precision. Longer sample runs tend to be more unstable (TS2) because of the drift in energy fluence of the CO_2 laser.

2. Compositions of experimental glasses

Table S2: Electron microprobe analyses of experimental peridotite glasses, with elemental abundances expressed as *wt.* % oxide.

Sample	**SiO_2**	**Al_2O_3**	**$FeO^{(T)}$**	**MgO**	**CaO**	**Na_2O**	**K_2O**	**SO_2**	**Total**
Per-fO_2 (1)	47.04±0.21	4.34±0.06	8.38±0.17	37.61±0.10	2.02±0.02	0.01	0.00	0.00	99.39
Per-fO_2 (2)	46.69±0.11	4.39±0.03	8.53±0.08	37.81±0.15	2.07±0.02	0.01	0.00	0.01	99.49
Per-fO_2 (3)	46.61±0.22	4.38±0.05	8.63±0.09	37.79±0.12	2.07±0.02	0.01	0.00	0.00	99.49
Per-fO_2 (6)	46.72±0.25	4.31±0.05	8.58±0.09	37.68±0.13	2.07±0.04	0.00	0.00	0.01	99.36
Per-fO_2 (7)	46.75±0.22	4.36±0.04	8.71±0.25	37.66±0.10	2.07±0.01	0.00	0.00	0.00	99.54
Per-fO_2 (8)	46.06±0.14	4.39±0.04	8.66±0.07	38.13±0.13	2.08±0.02	0.00	0.00	0.00	99.32
Per-fO_2 (9)	46.11±0.26	4.37±0.05	8.21±0.17	38.79±0.06	1.96±0.01	0.00	0.00	0.00	99.43
Per-fO_2 (10)	46.71±0.15	4.43±0.04	8.47±0.15	37.80±0.30	2.11±0.03	0.00	0.00	0.01	99.51
Per-fO_2 (11)	46.22±0.28	4.42±0.04	7.89±0.13	38.91±0.18	2.12±0.02	0.00	0.00	0.00	99.55
Per-fO_2 (12)	46.53±0.12	4.45±0.08	7.80±0.08	38.52±0.16	2.15±0.02	0.00	0.00	0.00	99.44
Per-TS1	46.45±0.16	4.32±0.05	8.87±0.13	37.62±0.10	2.04±0.02	0.01	0.00	0.01	99.30
Per-TS2	46.50±0.11	4.36±0.05	8.56±0.09	38.01±0.18	2.08±0.02	0.00	0.00	0.01	99.51

3. Treatment and quantification of XANES spectra

Normalised XANES spectra of peridotite glasses

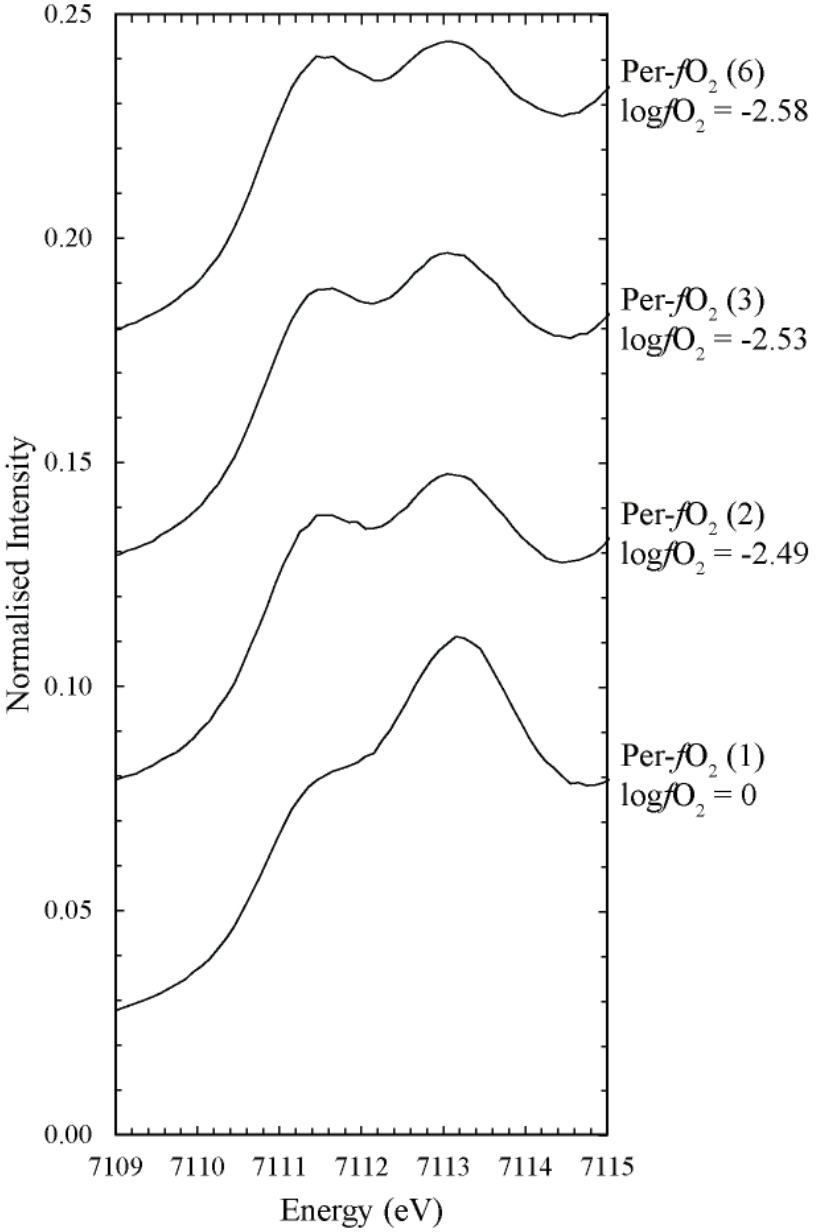

Fig. S2. Fe K-edge XANES pre-edge feature of oxidised glasses. Normalised (to 1) absorption spectra of Fe K-edge XANES depicting the pre-edge feature in the four most oxidised peridotite glasses (as labelled on the figure), scans offset vertically for clarity.

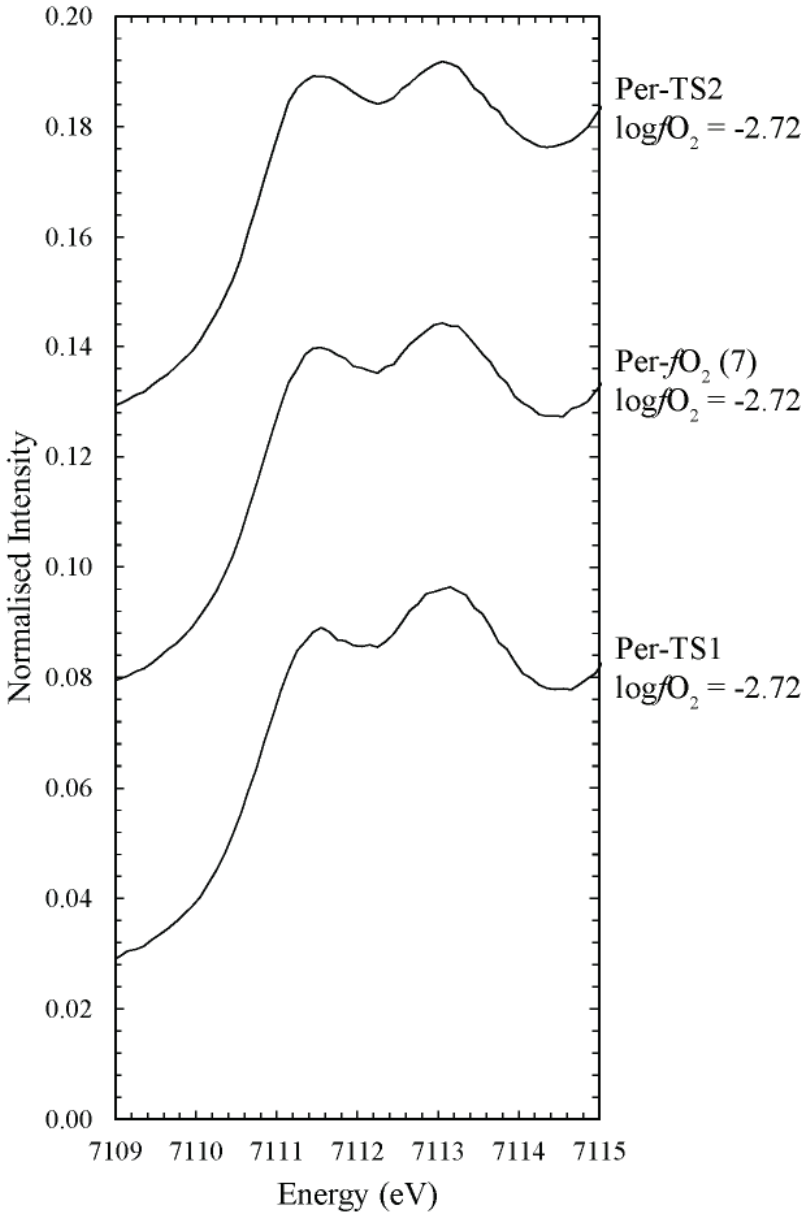

Fig. S3. Fe K-edge XANES pre-edge feature of intermediate glasses. Normalised (to 1) absorption spectra of Fe K-edge XANES depicting the pre-edge feature in the three 'time-series' experiments (as labelled on the figure), scans offset vertically for clarity.

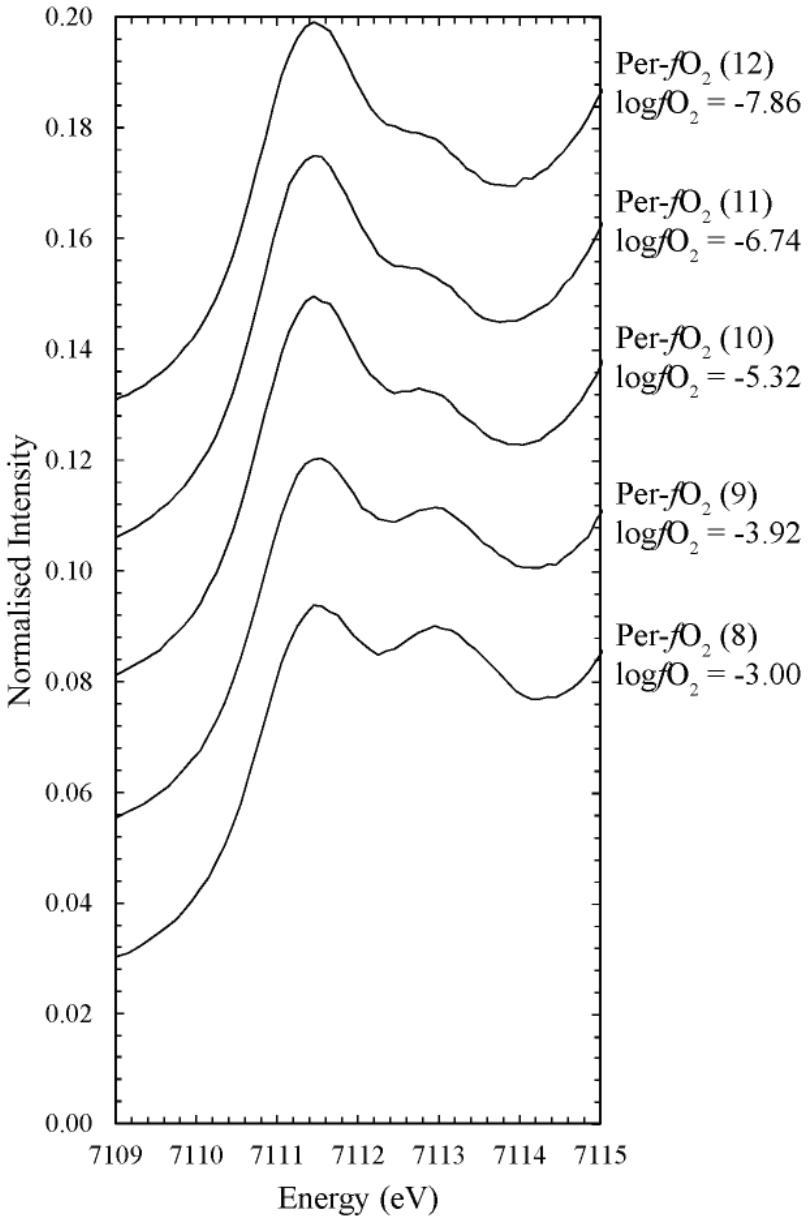

Fig. S4. Fe K-edge XANES pre-edge feature of reduced glasses. Normalised (to 1) absorption spectra of Fe K-edge XANES depicting the pre-edge feature in the five most reduced peridotite glasses (as labelled on the figure), scans offset vertically for clarity.

Calculation of $Fe^{3+}/\sum Fe$ ratios from XANES spectra of peridotite glasses

In order to calculate the $Fe^{3+}/\sum Fe$ ratio of the peridotite glasses, two features of the XANES spectra, the 0.8 edge energy (hereafter, 'Edge') and the centroid energy of the pre-edge feature (1s→3d electron transition; hereafter 'Centroid') are compared with those measured in synthetic Mid-Ocean Ridge Basalt (MORB) glasses, whose $Fe^{3+}/\sum Fe$ ratio is calibrated by independent means, namely, Mössbauer spectroscopy (*31*).

The XANES spectra of both the peridotite glasses and the MORB glasses were collected during the same analytical session at beamline 13IDE, Advanced Photon Source, Argonne National Laboratories (IL, USA). As such, the Edge and Centroid energies of the MORB glasses differ from the values given in ref. (*31*), their Table 2, due to a systematic offset in the energy calibration of 1.2±0.1 eV between beamline I18, Diamond Light Source, Oxford, UK and beamline 13IDE. As such, in this study, the energy calibration is internally consistent between MORB glass standards and peridotite glass samples. As the glasses are the same samples analysed in ref. (*31*), both $Fe^{3+}/\sum Fe$ and fO_2 of the MORB standard glasses are known (their Table 2).

To calculate the $Fe^{3+}/\sum Fe$ of the peridotite glasses, a global fit to the recorded Edge and Centroid energy values as a function of $Fe^{3+}/\sum Fe$ in the MORB glasses was performed. In this model, we derive expressions relating the Edge and Centroid energies to the $Fe^{3+}/\sum Fe$ values determined by the Mössbauer-based model global fit of ref. (*31*) (their Table 2). In order to do so with the least misfit, one must consider

i) The appropriate peak shape (Gaussian, Lorentzian, or a combination) to fit the Fe^{2+} and Fe^{3+} contributions to the pre-edge Centroid energy
ii) A functional form relating the Edge energy and Centroid energy to $Fe^{3+}/\sum Fe$

We therefore test several models, including fits using 2 Gaussian peaks, 2 Lorentzian peaks, and 1 Lorentzian and 1 Gaussian to the Centroid energy; and *n*-order polynomials (n = 3, 4) to quantify the relationship between n and $Fe^{3+}/\sum Fe$, by minimising the misfit to the objective function:

$$\chi^2 = \sum \frac{(Edge_{meas} - Edge_{calc})^2}{\sigma(Edge)} + \sum \frac{(Centroid_{meas} - Centroid_{calc})^2}{\sigma(Centroid)} \quad \text{(S1)}$$

Where 'Edge' and 'Centroid' are in eV and σ is their associated standard deviation, in eV. For the synthetic tests, we make the transformation 'Centroid' = $Centroid_{meas}$ – 7111 eV and 'Edge' = $Edge_{meas}$ – 7120 eV, in order to make the minimisation more tractable. The results of these tests are presented in Table S3, below.

Table S3. Results of synthetic tests with XANES spectra of the MORB glasses of ref. (*31*) used to determine the goodness of fit of polynomial functions relating (A) $Fe^{3+}/\sum Fe$ to 0.8 Edge Energy (B) $Fe^{3+}/\sum Fe$ to Centroid Energy and (C) $Fe^{3+}/\sum Fe$ (Centroid energy) to $Fe^{3+}/\sum Fe$ (0.8 Edge Energy).

MORB glasses (*31*)		A) $Fe^{3+}/\sum Fe$ *vs.* 0.8 Edge Energy		B) $Fe^{3+}/\sum Fe$ *vs.* Centroid Energy				C) $Fe^{3+}/\sum Fe$ (Centroid Energy) *vs.* $Fe^{3+}/\sum Fe$ (0.8 Edge Energy)		
	a0	-0.016	b0	-0.78	-0.61	-0.76	c0	-2.24	-1.18	-1.61
	a1	0.150	b1	1.34	1.44	1.48	c1	2.74	2.14	1.99
	a2	-0.008	b2	-0.64	-0.88	-0.83	c2	0.19	0.22	0.39
	a3		b3	0.17	0.25	0.23	c3			

Data		Misfit (3 term)	Misfit (4-term)			Misfit (3-term)		
$Fe^{3+}/\sum Fe$	σ		2 Gau	2 Lor	1 Gau & 1 Lor	2 Gau	2 Lor	1 Gau & 1 Lor
0.775	0.010	-1.75	1.16	1.06	1.16	0.18	0.24	0.15
0.662	0.010	1.39	-0.03	-0.70	-0.94	-0.06	-0.09	-0.11
0.524	0.010	1.43	-2.65	-1.17	-1.06	-0.21	-0.22	-0.15
0.404	0.020	0.33	-0.73	-0.34	-0.22	-0.10	-0.14	-0.09
0.251	0.007	0.65	3.89	2.54	2.53	0.21	0.20	0.16
0.162	0.006	-0.03	0.46	0.04	-0.46	0.09	0.15	0.08
0.098	0.005	-0.81	-0.83	-1.86	-1.72	0.05	0.07	0.05
0.059	0.004	-0.16	1.11	1.05	0.64	0.03	0.05	0.04
0.034	0.003	0.04	-0.52	-0.79	0.14	-0.04	-0.04	-0.02
0.019	0.002	-2.95	-0.52	0.70	0.31	-0.02	-0.02	0.00
0.011	0.001	-0.44	6.29	4.38	3.93	-0.03	-0.07	-0.04
0.006	0.001	1.89	-6.41	-4.63	-4.13	-0.12	-0.13	-0.10
			Global misfit (χ^2)					
3 term		**20.68**	118.5	104.5	68.4	0.16	0.23	**0.14**
4 term		8.00	107.4	55.8	**46.0**	0.03	0.02	0.02

* Misfit relative to the MORB glass data is shown for the different peak forms for the 4-term polynomial (Centroid Energy) and a 3-term polynomial (0.8 Edge Energy), with global misfit shown for both 3- and 4-term polynomials. Bold text represents the calibration chosen.

In finding a function to fit the dependence of Edge energy on $Fe^{3+}/\sum Fe$ (synthetic test A), the misfit improves only marginally from the 3- to 4-term polynomial, and is already low in both cases (<21). This relates to a mean offset of calculated $Fe^{3+}/\sum Fe$ compared to measured values of ±0.005. When compared to the $Fe^{3+}/\sum Fe$ determined by Mössbauer spectroscopy, the 1 Gaussian and 1 Lorentzian peak fits to the Centroid Energy yield lower (i.e., better) misfit to the observed $Fe^{3+}/\sum Fe$ for both the 3-term and 4-term fits (synthetic test B). The global χ^2 of 46.0 in the 4 term fit reflects an absolute uncertainty in $Fe^{3+}/\sum Fe$ of ±0.006. Moreover, the 1 Gaussian + Lorentzian peak fit produced $Fe^{3+}\sum Fe$ values that were in closest agreement with the 3-term polynomial fit to the 0.8 Edge energy (synthetic test C), and were therefore adopted throughout. The misfit between the observed and calculated Centroid energy improves markedly when passing from a 3-term to a 4-term polynomial (Table S3). Therefore, the 4-term and 3-term polynomials are taken to functionally fit the Centroid energy and the Edge energy, respectively:

$$\frac{Fe^{3+}}{\sum Fe}_{calc} = a_0 + a_1(Edge_{meas} - 7120) + a_2(Edge_{meas} - 7120)^2 \quad \text{(S2)}$$

$$\frac{Fe^{3+}}{\sum Fe}_{calc} = b_0 + b_1(Cent_{meas} - 7111) + b_2(Cent_{meas} - 7111)^2 + b_3(Cent_{meas} - 7111)^3 \text{ (S3)}$$

Best fit values yield for a_0 = -0.0157, a_1 = 0.1495, a_2 = 0.0083 and for b_0 = -0.7594, b_1 = 1.4792, b_2 = -0.8300, b_3 = 0.2283. Once established, these expressions can be used in order to calculate the $Fe^{3+}/\sum Fe$ ratios of the peridotite glasses from their measured Centroid and Edge energies.

However, the use of basaltic glasses to calibrate glasses of peridotitic composition is not necessarily substantiated *a priori*, as XANES spectra are not only sensitive to the oxidation state of Fe, but also to its overall bonding environment, which is influenced by composition (*83*). The composition of the synthetic MORB glass used for the standards is given in ref. (*31*), and is SiO_2 (52.0 wt. %), Al_2O_3 (16.1 wt. %), CaO (12.4 wt. %), $FeO^{(T)}$ (10.0 wt. %), MgO (8.2 wt. %) and TiO_2 (1.3 wt.%), which differs notably in its higher Al_2O_3, CaO and lower MgO contents compared to the peridotite glass (Table S2). Moreover, the Edge energy can be influenced by self-absorption depending on the mean atomic number of the medium through which the X-rays pass. However, the predominant contribution affecting this shift is the iron content of the glass itself, and typically only above the edge energy (*84*). Therefore, it may be expected that such a $Fe^{3+}/\sum Fe$ edge/centroid energy calibration would hold for glasses with similar iron contents, as in the MORB glass (10.0 *wt.* % $FeO^{(T)}$) and peridotite glass (8.44 *wt. %* $FeO^{(T)}$).

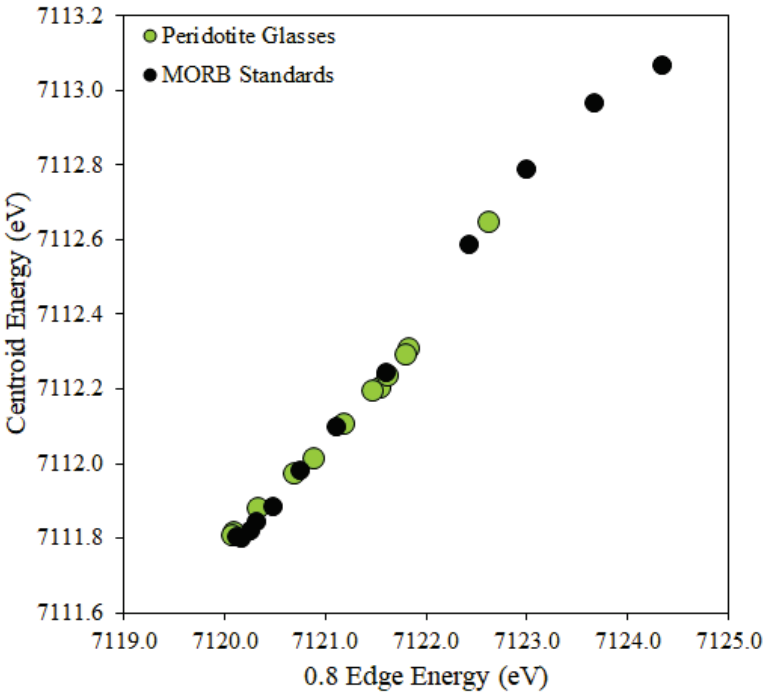

Fig. S5. Centroid *vs.* Edge energy of peridotite- and MORB glasses. The Centroid energy plotted against the 0.8 Edge energy for both the unknown peridotite glasses (green circles) and the calibration MORB glasses (black). The concurrence of the two series indicates that there is no systematic effect of composition on the relationship between the two quantities, meaning their variation is solely a function of $Fe^{3+}/\sum Fe$ ratio.

In order to evaluate the suitability of the MORB glasses as calibration standards for peridotite glasses, the relationship between measured Centroid- and Edge energies for each glass is plotted in Fig. S5. As evidenced from Fig. S5, the 'unknown' peridotite glasses fall on the same Centroid Energy – Edge Energy relationship defined by the MORB glasses of ref. (*31*). As such, the equations relating $Fe^{3+}/\sum Fe$ to both Centroid energy and Edge energy can be used in tandem to more precisely determine

$Fe^{3+}/\sum Fe$ in the peridotite glasses. These $Fe^{3+}/\sum Fe$ ratios are then related to the logfO_2 calculated for the individual gas mixture at 1900°C, and are shown in Table S4.

Table S4. A summary of experimental conditions of peridotite and MORB glasses, together with their determined 0.8 Edge and Centroid energies measured at 13IDE, and the $Fe^{3+}/\sum Fe$ ratios derived from eq. S2 and S3 (peridotite glasses) and reported in ref. (*31*), their Table 2 (MORB glasses).

Sample	Temperature (°C)	logfO_2	0.8 Edge Energy (eV)	Centroid Energy (eV)	$Fe^{3+}/\sum Fe$
Peridotite glasses (this work)					
Per-fO_2 (1)	1900±21	0.00	7122.624	7112.648	0.440±0.008
Per-fO_2 (2)	1893±40	-2.49	7121.833	7112.310	0.277±0.013
Per-fO_2 (3)	1861±29	-2.53	7121.792	7112.292	0.269±0.015
Per-fO_2 (6)	1878±23	-2.58	7121.547	7112.206	0.226±0.013
Per-TS1	1851±13	-2.72	7121.780	7112.291	0.267±0.013
Per-fO_2 (7)	1866±13	-2.72	7121.622	7112.235	0.240±0.013
Per-TS2	1875±41	-2.72	7121.460	7112.167	0.217±0.012
Per-fO_2 (8)	1924±13	-3.00	7121.184	7112.106	0.172±0.006
Per-fO_2 (9)	1902±15	-3.92	7120.885	7112.015	0.124±0.006
Per-fO_2 (10)	1900±21	-5.32	7120.335	7111.879	0.045±0.015
Per-fO_2 (11)	1896±16	-6.74	7120.085	7111.815	0.019±0.010
Per-fO_2 (12)	1839±17	-7.86	7120.079	7111.807	0.014±0.009
*MORB glasses (ref. (31))**					
MORB0	1400±2	0.00	7124.353	7113.065	0.775±0.010
MORB-1	1400±2	-1.00	7123.685	7112.962	0.662±0.010
MORB-2	1400±2	-2.00	7123.010	7112.865	0.524±0.010
MORB-3.07	1400±2	-3.07	7122.433	7112.433	0.404±0.020
MORB-4	1400±2	-4.00	7121.610	7112.239	0.251±0.007
MORB-5	1400±2	-5.00	7121.120	7112.095	0.162±0.006
MORB-6	1400±2	-6.00	7120.756	7111.978	0.098±0.005
MORB-7	1400±2	-7.00	7120.491	7111.833	0.059±0.004
MORB-8	1400±2	-8.00	7120.326	7111.841	0.034±0.003
MORB-9	1400±2	-9.00	7120.268	7111.815	0.019±0.002
MORB-10	1400±2	-10.00	7120.180	7111.796	0.011±0.001
MORB-11	1400±2	-11.00	7120.132	7111.801	0.006±0.001

*Glasses are the same as those measured in ref. (*31*). XANES spectra were re-collected at the same time as the peridotite glass samples in order to determine the Edge- and Centroid energies. The $Fe^{3+}/\sum Fe$ contents are taken from ref. (*31*), as quantified by best fits to fO_2-$Fe^{3+}/\sum Fe$ systematics determined by Mössbauer spectroscopy.

Three experiments were run for different durations at the same temperature and under the same gas mixture in order to assess the effect of run time on the observed $Fe^{3+}/\sum Fe$, and therefore the time for the melt to equilibrate with the gas mixture at high temperature. The samples subjected to the time series test were labelled Per-TS1 (10 s), Per-fO_2 (7) (30 s) and Per-TS2 (120 s), and their calculated $Fe^{3+}/\sum Fe$ ratios are shown plotted against run duration (Fig. S6).

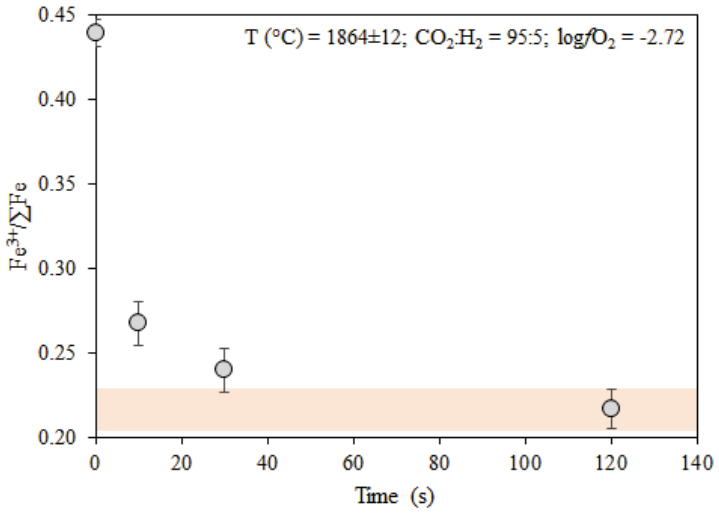

Fig. S6. Time series evolution of $Fe^{3+}/\sum Fe$ in peridotite glasses. Variation in the measured $Fe^{3+}/\sum Fe$ of quenched peridotite liquids as a function of time at constant temperature (1864±12) and logfO_2 (-2.72). The initial value of 0.440±0.008 comes from the fact that all glasses were first pre-equilibrated in pure O_2 at 2173 K prior to re-equilibration at the desired fO_2.

Because all glasses were pre-melted first in pure oxygen, the initial $Fe^{3+}/\sum Fe$ of the starting glass is given by sample Per-fO_2 (1), with $Fe^{3+}/\sum Fe$ = 0.440±0.008. Sample Per-TS1, run for 10 s, records resolvably higher $Fe^{3+}/\sum Fe$, 0.267±0.011, than either of the longer duration experiments under the same conditions (Per-fO_2 (7) and Per-TS2), with 0.240±0.013 and 0.217±0.012, respectively. This value lies intermediate between those recorded by the starting glass and the longer run durations, and, importantly, is also higher than that determined in sample Per-fO_2 (6), 0.226±0.013, run at marginally higher oxygen fugacity (logfO_2 = -2.58). Taken together, these features are indicative of incomplete equilibration of the melt with the gas mixture after 10 s at ~2150 K in sample Per-TS1. By contrast, the experiments run at 30 s and 120 s have $Fe^{3+}/\sum Fe$ within uncertainty of one another, and within uncertainty of Per-fO_2 (6). This suggests the melt and gas mixture equilibrate after ~ 30 s.

In order to better quantify the expected equilibration time, the diffusion timescale can be estimated from:

$$t = r^2/D$$

where t = time in (s), r = the radius of the melt sphere (0.001 m), and D = the diffusion coefficient of Fe. Experimental data suggest that D should vary as a function of composition and temperature (*85*). Here, we obtain a value of D_{Fe} from extrapolations based on basaltic compositions in air to 2173 K with an SiO_2 mole fraction of 0.4 for the peridotite liquid, yielding logD_{Fe} -6.73 (ref. (*86*); their eq. 86). Based on these models, full equilibration is achieved in ~6 s. However, our measurement times were counted from pyrometer temperatures measured at the surface of the bead, and hence the interior would have required longer timescales to reach the temperature measured at the surface. This thermal equilibration time, given the higher $Fe^{3+}/\sum Fe$ of sample Per-TS1, was likely of the order of 5 – 10 s. Once this temperature was reached throughout the bead, and considering that convection is also likely to play a role in melt homogenisation, sample run times > 15 s are sufficiently long to ensure complete equilibration of the melt with the imposed gas mixture.

4. Thermodynamic treatment of Fe^{2+}/Fe^{3+} as a function of oxygen fugacity

The fugacity of any given gas species is traditionally reported relative to the standard state of the pure ideal gas at 1 bar and the temperature of interest. When defined relative to this standard state, numerical values of fO_2 can change with temperature, for example in a silicate melt of constant composition including constant Fe^{3+}/Fe^{2+}, or in a H-C-N-O gas phase of constant composition. Therefore such numerical values of fO_2 are meaningless unless the temperature is specified. To avoid this complication, it is customary to switch to a standard state defined by a simple univariant equilibrium. Here we use for the standard state the equilibrium 2 Fe + O_2 = 2 FeO, for which ΔG^o (J/mol) = 488236 - 231.118 T + 16.948 T ln(T), where T is in K, from ref. (*87*). These thermochemical data are for solid Fe metal but liquid FeO, and, following common usage, is abbreviated IW (for Iron – Wüstite, the latter being the mineral name for crystalline $Fe_{1-x}O$). Hence $\log_{10}fO_2(IW) = -\Delta G^o/2.303RT$. Oxygen fugacity relative to the IW standard state are reported as ΔIW, where ΔIW = $\log_{10}fO_2$(O_2 standard state) – $\log_{10}fO_2$(IW). It is found empirically that values of ΔIW do not change greatly with temperature in condensed systems of fixed composition, at least under conditions relevant to magmatic processes.

At 2173 K, we obtain a value for the IW buffer of $\log fO_2$ = -6.47. This compares with $\log fO_2$ of -5.99 using our experimental calibration, $\log(Fe^{3+}/Fe^{2+}) = 0.252\times\log fO_2 + 0.096$ for an Fe^{3+}/Fe^{2+} = 0.0384 ($Fe^{3+}/\sum Fe$ = 0.037). Hence, the terrestrial mantle's $Fe^{3+}/\sum Fe$, were it to exist with the same ratio in liquid form, relates to an oxygen fugacity of ΔIW+0.48.

In order to understand the solution behaviour of iron in peridotite melts, we relate the free energy of reaction of the FeO and $FeO_{1.5}$ components in the melt to that of their pure oxides. For the redox reaction in the silicate melt, we can write:

$$FeO(l) + \tfrac{1}{4}O_2 = FeO_{1.5}(l), \quad \text{(S4)}$$

and for the reaction among pure oxides:

$$FeO(l) + \tfrac{1}{4}O_2 = \tfrac{1}{2}Fe_2O_3(l). \quad \text{(S5)}$$

Thermodynamic data for the Gibbs free energy of formation of the pure oxides from the elements can be found in the JANAF (*44*) and IVTAN (*88*) databases, and are shown in Table S5, below. In these databases, O_2(g) is defined as the reference state for oxygen, and has $\Delta G°_f = 0$ for all temperatures.

Table S5. Free energies of formation from the elements ($\Delta G°_f$) of iron oxides in kJ/mol.

	IVTAN		JANAF	
Temperature (K)	Fe_2O_3 (l,s)	FeO (l)	Fe_2O_3 (l,s)	FeO (l)
1700	-388.65	-165.24	-384.03	-163.83
1800	-364.26	-160.83	-364.53	-159.16
1900	-342.77	-155.94	*-343.65*	-153.83
2000	-321.81	-151.00	*-322.62*	-148.45
2100	-300.93	-146.07	*-301.59*	-143.09
2200	-280.13	-141.16	*-280.54*	-137.74
2300	-259.40	-136.27	*-259.49*	-132.41
2400	-238.73	-131.38	*-238.43*	-127.09

T_m (Fe_2O_3) = 1812 K

Italic = $\Delta G°_f$ calculated taking into account latent heat of fusion (eq. S6)

The JANAF tables report only ΔG°_f for crystalline Fe_2O_3 (hematite), and thus require a correction for the latent heat of fusion, which is performed according to the following relation:

$$\Delta_{fus}G_f^o = T_m\Delta_{fus}H_{T_m}^o - T\Delta_{fus}H_{T_m}^o \quad \text{(S6)}$$

We determine the value of $\Delta_{fus}H_{T_m}^o$ by comparing the ΔG°_f of the IVTAN and JANAF databases for solid hematite, and find $\Delta_{fus}H_{T_m}^o$ = 49 J/molK for Fe_2O_3. This is in perfect agreement with the 24.5 J/molK inferred by ref. (*38*) for $FeO_{1.5}$ from the interpolation of data for the heats of fusion of $AlO_{1.5}$ and $CrO_{1.5}$.

Through the relation $\Delta G_r = -RT\ln K$, we calculate the equilibrium constant of the reaction $\Delta G_r = 0.5\times\Delta G^\circ_f(Fe_2O_3) - \Delta G^\circ_f(FeO)$ (eq. S5). At 2173 K and 1 bar, we obtain the value for $\log K_{(JANAF)} = 0.095$ and $\log K_{(IVTAN)} = 0.009$. When compared with the $\log K$ obtained from the experimental data on the basis of the correlation of $\log fO_2$ with $\log(Fe^{3+}/Fe^{2+})$ (Fig. 2 of the main text) in quenched peridotite liquid, 0.096±0.053, we can obtain $\gamma FeO_{1.5}/\gamma FeO$ by the following relation:

$$\frac{\gamma FeO_{1.5}}{\gamma FeO} = \frac{\log K_{experiment}}{\log K_{JANAF/IVTAN}} \quad \text{(S7)}$$

We calculate values of 1.00±0.13 using the JANAF data and 1.22±0.15 using the IVTAN data.

5. Determination of the $Fe^{3+}/\sum Fe$ of a terrestrial magma ocean

In order to inform models of possible secondary atmospheric compositions to have formed from outgassing of a terrestrial magma ocean, we exploit the present-day estimates for *i)* the mantle's $Fe^{3+}/\sum Fe$ ratio and hence O content, and *ii)* the abundances of the other three major volatile elements, H, C, and N in the Earth's mantle. Specifically, their abundances in Earth's fictive 'primitive mantle' or bulk silicate Earth (BSE) is most pertinent to this question, as it reflected the composition of Earth's mantle prior its differentiation into crust and depleted mantle reservoirs (*24*, *89*).

Use of mantle peridotites to determine Fe^{3+}/Fe^{2+} of the magma ocean

Estimation of $Fe^{3+}/\sum Fe$ in peridotites derives from the weighted sum of $Fe^{3+}/\sum Fe$ of its constituent minerals. The three most comprehensive studies to this end are refs. (*40*, *90*) in xenolith suites and (*41*) in massif peridotites, in which Fe^{3+} contents of each of the five relevant mantle minerals (olivine, orthopyroxene, clinopyroxene, spinel and garnet) are determined from ^{57}Fe Mössbauer spectroscopy. Importantly, the 48 samples investigated by these authors cover a range of *i)* temperatures and pressures of equilibration *ii)* tectonic settings, and *iii)* fertility, that permit assessment of the degree to which these factors affect the $Fe^{3+}/\sum Fe$ of the whole rock (Table S6).

Table S6. Summary of data presented in refs. (*40, 41, 90*), showing selected features of whole rock peridotites from various localities and tectonic settings. Element oxides are presented in wt. %, T in °C and P in GPa. Refer to the original papers for methods.

Sample	Rock type	Locality	MgO	Fe_2O_3	FeO	CaO	Na_2O	T	P	$Fe^{3+}/\sum Fe$
Xenoliths										
Massif Central										
Fr1	spinel lherzolite	Landoz	37.5	0.30	7.56	3.64				0.034
Southeastern Australia										
84-402	spinel lherzolite, equigranular	Porndon	44.5	0.17	7.8	0.87		998	1.5	0.019
85-168	sp lherzolite, granoblastic tabular	Leura	42.4	0.20	9.8	1.20		1121	1.5	0.018
2905	sp lherzolite, protogranular tabular	Noorat	39.8	0.19	7.6	2.84		963	1.5	0.022
84-413	phlog. Wehrlite, secondary recrys	Noorat	36.1	0.41	8.5	2.60		874	1.5	0.042
BM134	amp-sp lherzolite, porphyroclastic	Bullenmeri	44.4	0.13	8.8	1.22		908	1.5	0.013
84-438	phlog. Wehrlite, porphyroclastic	Shadwell	39.8	0.42	8.5	3.71				0.043
Tanzania										
89-661	garnet lherzolite, coarse	Lashaine	48.1	0.07	6.8	0.94		1090	4.5	0.009
89-669	wehrlite, protogranular	Lashaine	43.7	0.09	9.5	1.75				
89-680	garnet harzburgite, coarse	Lashaine	45.9	0.14	6.6	0.81		1150	4.2	0.019
89-719	garnet harzburgite, coarse	Lashaine	47.7	0.07	6.8	0.55		1164	5.2	0.009
89-772	dunite, protogranular	Olmani	46.1	0.039	12.5	0.66		1120	2	0.003
89-773	harzburgite, protogranular	Olmani	49.1	0.09	5.97	0.11		1080	2	0.013
89-777	wehrlite, protogranular	Olmani	48.2	0.07	8.5	1.36				0.007
Southern Africa										
BD1140	garnet lherzolite, coarse, low T	Bultfontein	41.8	0.18	7.3	1.75		975	5	0.022
BD1150	garnet lherzolite, coarse, low T	Bultfontein	37.6	0.39	7.1	3.49		1141	7	0.047
BD1201	garnet lherzolite, coarse, low T	Wesselton	42.2	0.23	6.8	1.33		1007	6.3	0.030
BD1354	garnet websterite, coarse, low T	Matsoku	29.3	0.77	11.2	4.38		1294	9	0.058
F865	garnet harzburgite, w/diamond	Finsch	44.7	0.09	6.8	0.56				0.012
F556	garnet harzburgite, w/diamond	Finsch	40.7	0.16	9.2	0.96				0.015
FRB921	garnet websterite, coarse, low T	Premier	35.7	0.31	6.14	3.01		1055	4.2	0.043
FRB1350	sp-gt lherzolite, w/graphite	Premier	42.6	0.14	6.8	1.43		722	2.5	0.018
PHN5267	garnet lherzolite, sheared, high T	Premier	43.0	0.21	7.51	2.01				0.025
FRB909	garnet lherzolite, sheared, high T	Premier	42.1	0.21	8.1	1.63		1395	6.2	0.023

PHN5239	garnet lherzolite, sheared, high T	Premier	44.2	0.17	7.2	0.90	1431	7.1	0.021
Siberia									
UV417/89	garnet lherzolite, coarse, low T	Udachnaya	39.2	0.21	8.3	2.93	881	6.4	0.022
UV61/91	garnet lherzolite, sheared, high T	Udachnaya	44.6	0.14	7.3	1.68	1239	7.8	0.017
Massif Peridotites									
Beni Bousera									
bbI-32e	spinel lherzolite		39.31	0.145			947	1.5	
bbI-36	spinel harzburgite		45.23	0.04			920	1.5	
bbI-37a	spinel lherzolite		41.35	0.137			950	1.5	
bbI-37b	spinel lherzolite		41.35	0.130			950	1.5	
bbI-43	spinel lherzolite		39.89	0.184			1110	1.5	
bbII-13	spinel lherzolite		39.20	0.077			1137	1.5	
bbII-14	spinel lherzolite		44.73	0.034			1084	1.5	
bbIV-11	spinel harzburgite		46.22	0.084			930	1.5	
Ronda									
E3-126a	spinel lherzolite		44.59	0.051			915	1.5	
E3-126b	spinel lherzolite		44.59	0.054			915	1.5	
E3-208a	plagioclase lherzolite		42.24	0.088			929	1	
E3-208b	plagioclase lherzolite		42.24	0.098			929	1	
E3-227	spinel lherzolite		44.20	0.117			935	1.5	
E3-144	spinel lherzolite		39.07	0.224			948	1.5	
E3-148	spinel lherzolite		38.60	0.165			987	1.5	
Pyrenees									
Py-1	spinel lherzolite	Fontête Rouge	40.39	0.190			958	1.5	
Py-18	apatite-bearing sp lherzolite	Lherz	40.49	0.263			986	1.5	
Py-30a	spinel lherzolite	Lherz	40.28	0.197			833	1.5	
Py-30b	spinel lherzolite	Lherz	40.28	0.198			833	1.5	
Py-34	spinel lherzolite	Lherz	39.74	0.220			903	1.5	
Py-25	amphibole-bearing sp lherzolite	Caussou	40.71	0.279			849	1.5	

From Fig. S7a, b, it is clear that there is no dependence of $Fe^{3+}/\sum Fe$ on either the temperature or pressure of equilibration, a conclusion that holds irrespective of whether the aluminous phase is spinel (P ~ 1.5 GPa) or garnet (P > 2 GPa). This is also true of samples that have similar chemical composition and equilibration temperature, such as sample 84-402 with T (°C) = 998 and P (GPa) = 1.5, a spinel lherzolite with 44.5 wt. % MgO from Southeastern Australia and sample UV61/91 with T (°C) = 1239 and P (GPa) = 7.8, a sheared garnet lherzolite with 44.6 wt. % MgO from Udachnaya, Siberian craton. The former sample has $Fe^{3+}/\sum Fe$ of 0.019, whereas the latter has 0.017. The effect of temperature is difficult to isolate, as many continental xenoliths fall along geotherms with similar temperature gradients of ~40 mW/m^2. Nevertheless, the sample FRB1350, a spinel-garnet lherzolite containing graphite from the Kaapvaal craton, with an equilibration temperature of 722 °C and a pressure of 2.5 GPa, and an MgO content of 42.6 wt. % has $Fe^{3+}/\sum Fe$ of 0.018. This $Fe^{3+}/\sum Fe$ is identical to that of a spinel lherzolite from Southeastern Australia, 85-168, with T = 1121 °C, P = 1.5 GPa and MgO = 42.4 wt. %. It should also be noted that these xenoliths come from rather different tectonic settings; from the stable Archean shields of the Kaapvaal (FRB1350) and Siberian (UV61/91) cratons (*91*) and from the Tertiary Newer Volcanic Province erupting above lithosphere of accreted Phanerozoic arc terranes (85-168 and 84-402) (*92*).

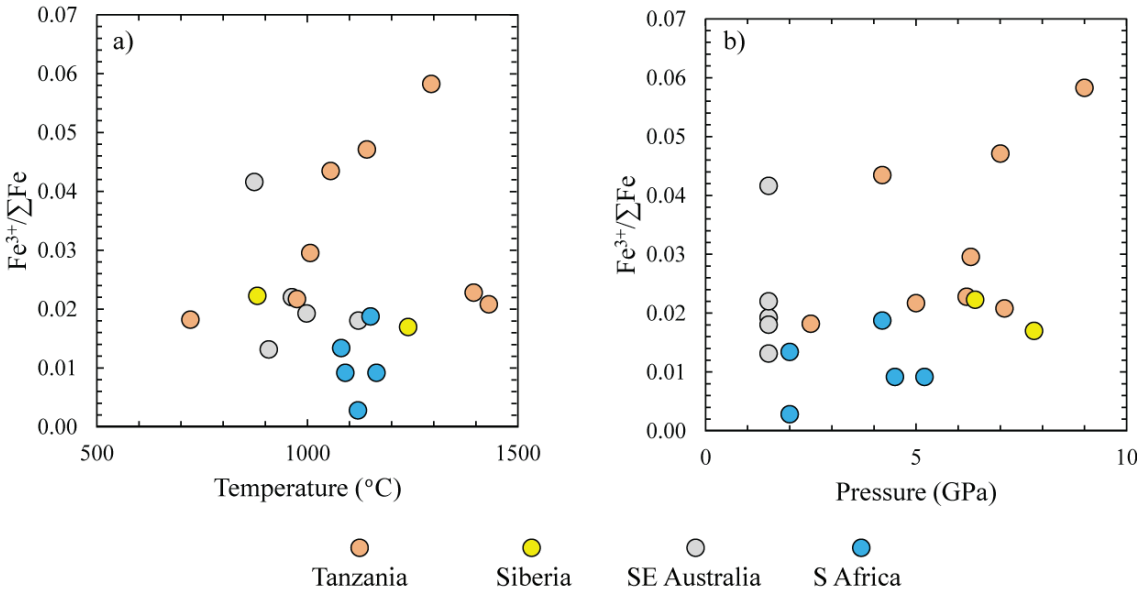

Fig. S7. Variation of $Fe^{3+}/\Sigma Fe$ of natural peridotite xenoliths with temperature and pressure. Data of refs. (*40, 41, 90*) illustrating the variation of $Fe^{3+}/\sum Fe$ in whole rock peridotites determined by measurements of individual minerals via Mössbauer spectroscopy with **a)** Temperature (°C) and **b)** Pressure (GPa). Samples are colour-coded according to their locality.

The observation that, for a given bulk composition, the temperature and pressure of equilibration (and tectonic setting) have no discernible effect on the $Fe^{3+}/\sum Fe$ is crucial in establishing the insensitivity of the ratio to any potential redox exchange with other multivalent species (Cr, H, C, and S, in particular). This suggests that either *i)* the oxygen fugacities of samples in the upper mantle are such that redox reactions between other multivalent species do not occur (i.e., the equilibrium constant of the reaction $H_2O = H_2 + ½O_2$ at mantle fO_2s always has high H_2O/H_2 ratios) or that *ii)* any small change in the ratios of other redox-sensitive species (e.g. H_2O/H_2, Cr_2O_3/CrO, CO_2/C) is buffered by Fe^{3+}/Fe^{2+} (*cf.* ref. (*40*)). On the basis of these observations, $Fe^{3+}/\sum Fe$ can be taken as a faithful record of the oxygen content of peridotite.

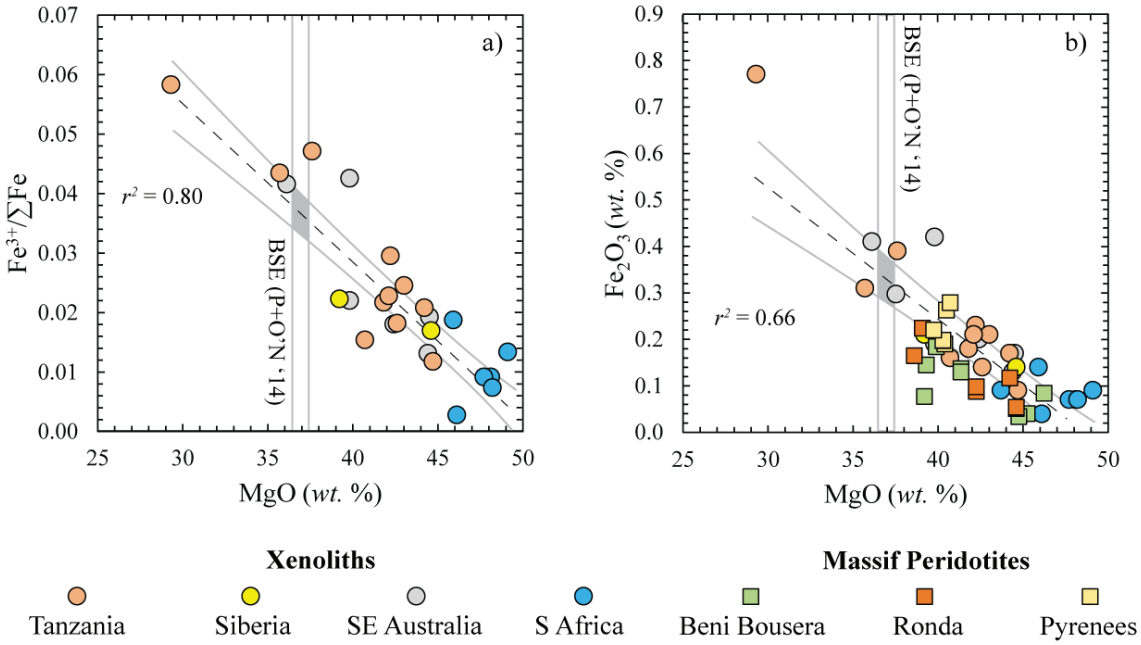

Fig. S8. The variation of a) $Fe^{3+}/\sum Fe$ and b) Fe_2O_3 (wt. %) with MgO (wt. %) in whole rock peridotites. Shown is the line of best fit (dashed black line) and its 95 % confidence envelope (grey curves). The MgO content of the BSE (*24*) is shown as a range demarcated by the grey vertical lines. The area of intersection gives the mean value and uncertainty thereof of the $Fe^{3+}/\sum Fe$ of the BSE (grey area). Data from refs. (*40, 41, 90*), see Table S6.

Examination of the dataset presented in Table S6 shows that $Fe^{3+}/\sum Fe$ covaries with indices of melt extraction; namely, the abundances of MgO, CaO and Na_2O in the peridotite whole rock (Fig. S8). Correlations with each of the element oxides defines an r^2 ~0.6 for the 20 pristine samples, with $Fe^{3+}/\sum Fe$ decreasing as the amount of basaltic component in the rock decreases (*40*, *90*). Partial melting of the mantle produces melts with a higher $Fe^{3+}/\sum Fe$ ratio than in their source peridotite, due to the high contribution of clinopyroxene and spinel to the melting reactions at low pressures (*93*, *94*) and the higher incompatibility of Fe^{3+} relative to Fe^{2+} in mantle minerals (*71*). By mass balance, therefore, $Fe^{3+}/\sum Fe$ in the residuum must decrease. These correlations can then be used to calculate the $Fe^{3+}/\sum Fe$ of a fictive BSE composition, and yield, based on MgO, $Fe^{3+}/\sum Fe = 0.035$, for CaO, $Fe^{3+}/\sum Fe = 0.036$ and for Na_2O, $Fe^{3+}/\sum Fe = 0.036$, and hence an average of 0.036±0.001, $n = 20$. As all samples lie on the same trend, we use the entire dataset of ref. (*40*) to derive the relationship:

$$\frac{Fe^{3+}}{\Sigma Fe}(\%) = 13.7 \pm 1.1 - 0.27 \pm 0.03 \times MgO\ (wt.\%); r^2 = 0.80, n = 26 \quad \text{(S8)}$$

At the MgO content of the BSE, 36.77±0.44 *wt.* % (*24*), eq. (S10) gives $Fe^{3+}/\sum Fe$ of 0.037±0.005, propagating errors on both the BSE MgO content and the 95 % confidence interval on the regression (Fig. S8).

With the inclusion of massif peridotite samples (*41*) allows for derivation of the relationship:

$$Fe_2O_3\ (wt.\%) = 1.37 \pm 0.13 - 0.028 \pm 0.003 \times MgO\ (wt.\%); r^2 = 0.66, n = 48 \quad \text{(S9)}$$

Which, despite the greater number of samples, has a lower correlation coefficient. At the MgO content of the BSE, this expression yields Fe_2O_3 (*wt.* %) = 0.33±0.06. Given the well-known value of the FeO content of the BSE, 8.1±0.1 *wt.* %, this translates into an $Fe^{3+}/\sum Fe$ of 0.037±0.007, consistent with estimates from eq. (S8).

Use of Mid-Ocean Ridge Basalt (MORB) glasses to constrain the Fe^{3+}/Fe^{2+} of their mantle sources

The $Fe^{3+}/\sum Fe$ ratios of MORB glasses have been determined by XANES spectroscopy (*31*) with results that are in agreement with previous wet-chemical determinations (*51*). The mean $Fe^{3+}/\sum Fe$ value is 0.11 and shows a weak negative correlation with the MgO content of the glass (*39*). Because MORB glasses have evolved from their parental magmas (*i.e.,* they have Mg#s lower than that expected for equilibrium with Fo_{90} olivine, their $Fe^{3+}/\sum Fe$ ratios cannot be directly be used to determine those of their mantle sources. Assuming the 'Replenish-Fractionate-Tap' model of MORB genesis gives a parental melt at 10.4 *wt.* % MgO with 0.61 ± *wt.* % Fe_2O_3 (*39*) (their Fig. 1). Alternatively, an empirical extrapolation to calculate their Fe_2O_3 contents at a melt Mg# of 0.72, yields values of 0.73±0.18 *wt.* % (*31*).

The corresponding Fe_2O_3 content of the mantle source can then be estimated by applying the non-modal batch melting equation, a fair approximation to the physically more realistic polybaric accumulated fractional melting. The equation for batch melting is

$$C_o = C_l(D + F(1 - P)) \quad \text{(S10)}$$

where C_o and C_l are the concentrations of Fe_2O_3 in the source, and liquid, respectively, D is its bulk partition coefficient between solid and liquid, equated at each melt fraction F. Here, the non-modality of melting is applied by adopting P according to the measured values as a function of F from (*39*), yielding $C_o/C_l = 2.9$ at $F = 0.2$, giving $C_o = 0.21$±0.06 or 0.25±0.06 *wt.* % Fe_2O_3.

Assuming the mantle source of MORB contains 8.1 *wt.* % $FeO^{(T)}$ (*95*), these Fe_2O_3 contents imply $Fe^{3+}/\Sigma Fe$ ratios of 0.028±0.007. For the 'Replenish-Tap-Fractionate' model of MORB genesis and the data of (*31*), a value of 0.21±0.06 wt. % Fe_2O_3 in the MORB source was estimated (*39*), yielding $Fe^{3+}/\Sigma Fe$ = 0.023±0.006. Because the MORB source mantle, on the basis of its trace element composition, is residual following ~3 – 5 % melt extraction (*95*), these $Fe^{3+}/\Sigma Fe$ are minimum estimates. Because of their agreement with direct measurements of $Fe^{3+}/\Sigma Fe$ in peridotites, whose composition enables determination of that in the BSE, we adopt $Fe^{3+}/\Sigma Fe$ = 0.037±0.005 as the nominal value of the terrestrial magma ocean.

6. Thermodynamic models of atmospheric composition

Use of the contemporary BSE abundances to calculate a primitive atmosphere implies that the Earth had already attained in present-day complement of H, C, N, and O by the time of the giant impact. By contrast, should the late veneer, thought to represent ~0.5 wt. % of the Earth's mass, have delivered the bulk of the Earth's volatile budget (*4*), then the post giant-impact magma ocean would have contained fewer volatiles, and likely in different ratios, than exist in the BSE today. However, due to the contrasting identities invoked for the chondritic meteoritic material (*4*, *70*, *96*) thought to have comprised the late veneer, back-calculating the volatile composition of a terrestrial magma ocean is uncertain. As such, while the equivalence of the present-day BSE volatile budget with that of the early Earth cannot be conclusively demonstrated, it remains our strongest constraint as to the composition of the Hadean Earth.

Recent estimates for the composition of the BSE converge relatively well upon the abundances of H, C and N (Table S7).

Table S7: Recent estimates of the abundances (in mass %) of the major volatiles H, C and N in the bulk silicate Earth (BSE), and their associated H/C and H/N ratios by mass and by moles.

	BSE (*24*)	BSE (*53*)
Abundances (mass %)		
H	0.0120±0.0024	0.0079±0.0010
C	0.0100±0.050	0.014±0.004
N	0.0002±0.0001	0.00028±0.00006
Ratios		
H/C (mass)	1.2	0.56
H/C (moles)	14.4	6.76
H/N (mass)	60	28.2
H/N (moles)	840	395

Should the magma ocean quantitatively degas its entire H, C, and N budget, it would produce partial pressures (in bar) of p_{H_2O} = 832.6, p_{CO_2} = 282.7 and p_{N_2} = 1.54 for the BSE estimates of ref. (*24*), and p_{H_2O} = 547.4, p_{CO_2} = 395.8 and p_{N_2} = 2.16 for the more recent model of ref. (*53*). In both cases, however, H would be expected to be the dominant component, both by moles and by mass, in a terrestrial atmosphere, with N_2 contributing only as a minor component, at most ~2 bar of pressure. These estimates, however, assume negligible solubility of these elements in a silicate (i.e., peridotitic) magma ocean. In practice, each of these elements are soluble to varying degrees in silicate liquid and hence their associated partial pressures in the atmosphere will decrease accordingly.

Solubility laws depend on the speciation of the element in question, both in the liquid silicate and in the gaseous phase (*8*, *56*). The oxygen fugacity of the magma ocean as constrained by $Fe^{3+}/\sum Fe$ of natural peridotites, combined with that determined by XANES spectroscopy of peridotite liquids, is equal to ΔIW+0.5. These mildly oxidising conditions allow some simplifying assumptions to be made as to the speciation of H, C and N in silicate melts. Ref. (*97*) showed that dissolved H_2 in basaltic silicate melts in equilibrium with a vapour phase with fH_2 between 166 and 68163 bar only becomes

important at oxygen fugacities below IW. By the same token, ref. (*57*) found evidence for the occurrence of $Fe(CO)_5$ and minor CH_4 in silicate melts of a lunar basaltic composition, but only at, or below, ΔIW-0.55. In a study of the solubility of N in silicate melts, dissolved N_2 was shown to be stable in a basaltic melt composition over a wide range of fO_2, down to the IW buffer (*56*).

Therefore, we presume that H dissolves as molecular H_2O and partially dissociates to OH in silicate melts (*58*):

$$H_2O(g) = H_2O(l) \text{ (S11)}$$

$$H_2O(l) + O(l) = 2OH(l), \text{ (S12)}$$

Because of the highly depolymerised melt composition, C is incorporated exclusively as the CO_3^{2-} anion (*98*):

$$CO_2(g) + O^{2-}(l) = {CO_3}^{2-}(l), \text{ (S13)}$$

and N is dissolved as molecular N_2 (*56*):

$$N_2(g) = N_2(l) \text{ (S14)}$$

The solubility of these elements in peridotite liquid can be estimated using expressions for the solubility of CO_3^{2-}, H_2O and N_2 in basaltic melts. There are, however, two caveats to be mindful of, *i)* existing calibrations are performed over a limited temperature range (800 ≤ T °C ≤ 1400 °C) and *ii)* the compositions do not reflect those of a peridotite liquid. As such, extrapolation of existing solubility laws to the conditions of the magma ocean, at 2173 K for a peridotite liquid, should be treated with caution. Nevertheless, there are features of the behaviour of H_2O and CO_3^{2-} in basaltic liquids evident from existing data that suggest these laws should provide a good estimate of their solubility in peridotite liquids. First, the temperature dependence of their solubilities has been shown to be weak (H_2O; (*99*)) or undetectable within experimental uncertainty (CO_3^{2-}; (*100*)). Furthermore, in the expression of (*54*) used to calculate water solubility, coefficients that take into account the mole fractions of the liquid oxides are included in order to account for the effect of composition of the silicate melt on H_2O solubility.

With these considerations in mind, the solubility of H_2O in peridotite liquid is calculated by (*54*):

$$2\ln X_{H_2O}^{melt} = \frac{a}{T} + \sum_i b_i X_i \left(\frac{P}{T}\right) + c \ln f_{H_2O}^{fluid} + d \text{ (S14)}$$

where $X_{H_2O}^{melt}$ and $f_{H_2O}^{fluid}$ are the mole fraction and fugacity of water in the melt and fluid, respectively, a = 2565, $b_{Al_2O_3}$ = -1.997, $b_{FeO^{(T)}}$ = -0.9275, b_{Na_2O} = 2.376, X_i refers to the oxide mole fraction, c = 1.171, d = -14.21, P is the total pressure in bars and T the temperature in Kelvin. We set $X_{FeO^{(T)}}$ = 0.08, $X_{Na_2O} = 0$ and $X_{Al_2O_3}$ = 0.04.

The solubility of CO_3^{2-} in peridotite liquid is calculated following the model of (*55*):

$$X_{{CO_3}^{2-}}^{melt}(P,T) = X_{{CO_3}^{2-}}^{melt}(P_0,T_0)\frac{f_{CO_2}^{gas}(P,T_0)}{f_{CO_2}^{gas}(P_0,T_0)}\exp\left\{\frac{-\Delta V_r^{o,melt}(P-P_0)}{RT_0}\right\} \text{ (S15)}$$

where R is the gas constant, $\Delta V_r^{o,melt} = (V_{{CO_3}^{2-}}^{o,melt}) - (V_{O^{2-}}^{o,melt})$ and $V_{{CO_3}^{2-}}^{o,melt}$ and $V_{O^{2-}}^{o,melt}$ are the standard molar volumes of CO_3^{2-} and O^{2-} in the silicate melt that are assumed to be independent of P and T over the range considered. Setting P_0 to 1 bar and T_0 = 1473 K, and $\Delta V_r^{o,melt}$ 23 cm^3/mol the best fit value of $X_{{CO_3}^{2-}}^{melt}$ = 3.8×10^{-7} or ~0.5 ppm (*55*).

The solubility of nitrogen as N_2 is the lowest of the three elements, and, above the IW buffer, is simply given according to Henry's law (*56*):

$$N^{melt}\ (ppm) = f_{N_2}^{gas}(0.0611 \pm 0.0149). \text{ (S16)}$$

where N^{melt} is the concentration of nitrogen in the melt in parts per million.

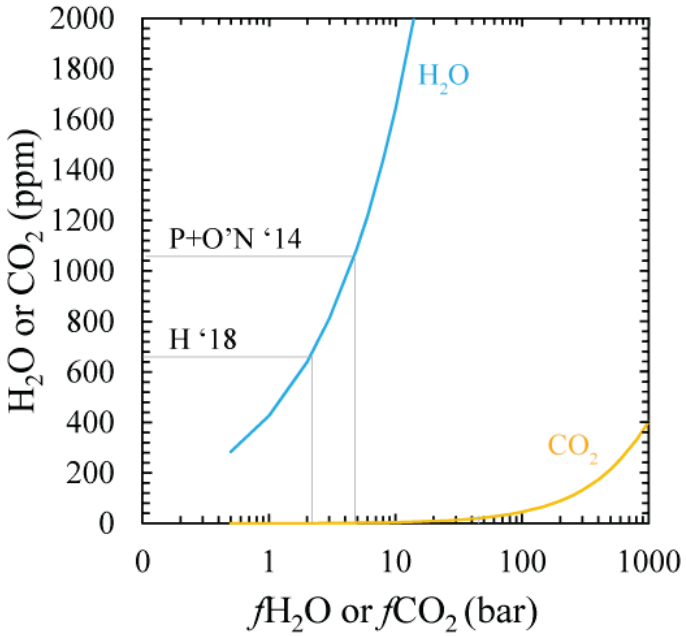

Fig. S9. Solubilities of H_2O and CO_2 in a terrestrial magma ocean. The solubility (in ppm) of H_2O (blue) and CO_2 (yellow) in a silicate melt of peridotite composition at 2173 K as a function of fH_2O and fCO_2 as calculated by the equations of refs. (*54*) and (*55*), respectively. The grey lines represent the BSE estimates of H_2O according to (*53*) (H '18) and (*24*) (P+O'N '14), predicting fH_2O of ~2.5 bar and 5 bar, respectively. Conversely, the fCO_2 calculated for a fully-degassing magma ocean of 62.5 bar and 41 bar yields 28.3 (ref. (*53*)) and 20.3 (ref. (*24*)) ppm CO_2 in the magma ocean. All fugacities by mass.

The H_2O solubility in the magma ocean is given by the point at which the BSE content of H_2O (Table S7) crosses the solubility curve defined by eq. S14 (Fig. S9). This occurs at only 2.5 bar H_2O for the composition of (*53*), and 5 bar for the composition of (*24*). At an fO_2 of ΔIW+0.5, the H_2O/H_2 ratio is calculated according to the following equation:

$$H_2(g) + \frac{1}{2}O_2(g) = H_2O(g) \text{ (S17)}$$

With a log$K$ of reaction at 2173 K of 3.21 assuming an ideal gas (*43*). This yields 0.2 bar of H_2 for 2.5 bar H_2O and 0.4 bar of H_2 for 5 bar H_2O (by mass). This equates to between 99.6 % and 99.4 % of the H_2O budget of the BSE being stored in the magma ocean. The final pressures of $\sum f(H_2O_x; x = 0 \text{ or } 1)$ are therefore between 2.7 and 5.4 bar (by mass).

For C, at ΔIW+0.5, the gas phase is predicted to have $fCO/fCO_2 \sim 3.5$, according to the reaction:

$$CO(g) + \frac{1}{2}O_2(g) = CO_2(g) \text{ (S18)}$$

for which the log$K$ is calculated to be 2.30 at 2173 K (*43*). Hence, fCO_2 is significantly lower than $\sum f(CO_x; x = 1 \text{ or } 2)$. In this case, it is assumed that the oxygen buffering capacity of the mantle far exceeds that of the atmosphere, such that the atmospheric fCO/fCO_2 is fixed at 3.5 (or 4.8 by moles).

For an initial C abundance of 0.014 % in the BSE, 62.5 bar of CO_2 and 221.1 bar of CO are present in a fully-degassed atmosphere of ref. (*53*) at ΔIW+0.5. This is equivalent to 287 ppm of CO and 81 ppm of CO_2 in the magma ocean. An fCO_2 = 62.5 bar, eq. S15 predicts a CO_2 solubility in the magma ocean of 28.3 ppm, or 35% of the CO_2 budget. In order to maintain fCO/fCO_2 = 3.5, it must also dissolve an appropriate amount of CO (though its speciation in the magma ocean is CO_3^{2-} given the excess buffering capacity of oxygen). There is some equilibrium amount of CO (likely in the form $Fe(CO)_5$ (*57*)) below ΔIW-0.55, but this is not considered here. This results in a final pressure of CO = 144 bar and CO_2 = 41 bar (by mass). An equivalent calculation for the BSE composition of ref. (*24*) yields 102.5 bar CO and 29 bar CO_2 (by mass).

For 2.16 bar of N_2, eq. S16 predicts an N content of the magma ocean of 0.13 ppm, or 5% of the total N budget. This quantity is smaller than the uncertainty in the abundance of N in the BSE (±0.6 ppm (*53*)), and so it is assumed that N_2 is present entirely in the atmosphere at fN_2 of 2.16 bar (*53*) or 1.56 bar (*24*).

The resultant total pressures in an atmosphere in equilibrium with a magma ocean at 2173 K are 138.5 bar with the BSE of (*24*), and 189.5 bar for the BSE composition of (*53*). The molar H/C and H/N ratios are 0.23 and 6.79 for the model of (*24*) and 0.07 and 2.25 using the BSE abundances of (*53*)

FactSage Atmosphere model

With this information, the speciation of a model magma ocean atmosphere with molar H/C and H/N combining the estimates of (*24*, *53*) estimates and a total pressure of 140 bar can be calculated using FactSage. The moles of all species are normalised to H = 1, yielding C = 4.3 and N = 0.17. The moles of O are adjusted such that the fO_2 gives a value equivalent to ΔIW+0.5 at 2173 K (10^{-6} bar), and, for this composition, is found to be 5.3. The initial total pressure is set to 140 bar, to reflect the sum of the CO, CO_2, H_2, H_2O and N_2 species predicted to be present at 2173 K. The speciation and fugacities of the stable gas species, along with any condensed phases, are then calculated by minimising the Gibbs free energy of the system using FactSage 7.3 (*61*) at a given temperature and pressure. It should be noted that these conditions initially exceed the critical point of H_2O (647 K and 221 bar) and of mixed CO_2-H_2O systems (*77*).

As our treatment deals only with pure phases (i.e., no real or solid solutions), the calculations are necessarily simplified upon precipitation of graphite and water. Furthermore, the calculations are made so as to approximate a closed system, in which the bulk composition is held constant, and interactions of the atmosphere with the magma ocean, crystalline silicates, or other solids are ignored. As such, reactions of high water vapour pressures with condensed phases to form hydrous minerals, or the dissolution of CO_3^{2-} into seawater are not treated and are beyond the scope of this work. Results of these calculations are discussed as Fig. 3 and in the main text.

Table S8-I. Fugacities (bar) of species in a real gas calculated according to FactSage simulating closed system cooling of a magma ocean at ΔIW+0.5 from 2173 K to 273 K with initial molar ratios of H/C = 0.22 and H/N = 5.8. Part I – 2173 K – 1473 K

Temp. (K)	2173	2123	2073	2023	1973	1923	1873	1823	1773	1723	1673	1623	1573	1523	1473
Gas (moles)	4.88	4.88	4.88	4.88	4.88	4.88	4.88	4.88	4.88	4.88	4.88	4.88	4.88	4.88	4.88
CO	101.8	101.7	101.6	101.5	101.4	101.3	101.1	101.0	100.8	100.7	100.5	100.3	100.1	99.9	99.7
CO_2	21.3	21.4	21.5	21.6	21.7	21.8	21.9	22.1	22.2	22.4	22.6	22.8	23.0	23.2	23.4
H_2O	7.3	7.2	7.1	7.0	6.9	6.8	6.7	6.5	6.4	6.3	6.0	5.9	5.7	5.4	5.2
H_2	6.9	7.0	7.1	7.2	7.4	7.5	7.6	7.8	7.9	8.1	8.3	8.5	8.7	8.9	9.1
N_2	2.4	2.4	2.4	2.4	2.4	2.4	2.4	2.4	2.4	2.4	2.4	2.4	2.4	2.4	2.4
O_2	1.0E-06	5.1E-07	2.4E-07	1.1E-07	4.8E-08	2.0E-08	8.1E-08	3.1E-09	1.1E-09	3.8E-10	1.2E-10	3.5E-11	9.7E-12	2.2E-12	5.2E-13
O	2.3E-06	1.2E-06	5.6E-07	2.6E-07	1.2E-07	5.1E-08	2.1E-08	8.3E-09	3.1E-09	1.1E-09	3.6E-10	1.1E-10	3.2E-11	8.5E-12	2.1E-12
CH_4	3.7E-09	5.2E-09	7.5E-09	1.1E-08	1.6E-08	2.5E-08	4.0E-08	6.4E-08	1.1E-07	1.8E-07	3.2E-07	5.8E-07	1.1E-06	2.2E-06	4.5E-06
NH_3	3.2E-06	3.6E-06	3.9E-06	4.4E-06	4.9E-06	5.4E-06	6.1E-06	6.9E-06	7.9E-06	9.1E-06	1.1E-05	1.2E-05	1.5E-05	1.7E-05	2.1E-05
Total P (bar)	139.8	139.8	139.8	139.8	139.8	139.8	139.8	139.8	139.8	139.9	139.8	139.8	139.8	139.8	139.8
Condensed phases															
Graphite (moles)															
Graphite (mass)															
Water (moles)															
Water (mass)															

Table S8-II. Fugacities (bar), in moles, of species in a real gas calculated according to FactSage simulating closed system cooling of a magma ocean at ΔIW+0.5 from 2173 K to 273 K with initial molar ratios of H/C = 0.22 and H/N = 5.8. Part II – 1423 K – 773 K.

Temp. (K)	1423	1373	1323	1273	1223	1173	1123	1073	1023	998	973	923	873	823	773
Gas (moles)	4.88	4.88	4.88	4.88	4.88	4.88	4.88	4.88	4.88	4.6478	4.374	3.8739	3.506	3.2723	3.1361
CO	99.4	99.2	98.9	98.6	98.3	97.9	97.6	97.2	96.8	84.1	69.2	52.2	22.9	11.2	4.9
CO_2	23.7	23.9	24.2	24.5	24.8	25.1	25.5	25.9	26.3	32.4	39.5	42.2	61.1	66.1	68.5
H_2O	5.0	4.7	4.4	4.1	3.8	3.5	3.1	2.8	2.4	2.9	3.7	5.2	6.9	8.5	9.9
H_2	9.3	9.6	9.9	10.2	10.5	10.8	11.2	11.5	11.8	11.2	10.4	8.8	7.0	5.3	3.7
N_2	2.4	2.4	2.4	2.4	2.4	2.4	2.4	2.4	2.4	2.4	2.4	2.3	2.4	2.4	2.4
O_2	1.1E-13	2.1E-14	3.3E-15	4.6E-16	5.3E-17	5.2E-18	4.1E-19	2.5E-20	1.2E-21	4.6E-22	1.7E-22	1.9E-23	1.3E-24	5.4E-26	1.4E-27
O	4.5E-13	8.8E-14	1.5E-14	2.3E-15	2.9E-16	3.2E-17	2.8E-18	2.0E-19	1.1E-20	3.1E-21	8.9E-22	5.3E-23	2.1E-24	5.3E-26	7.9E-28
CH_4	9.8E-06	2.3E-05	5.5E-05	1.5E-04	4.1E-04	1.3E-03	4.4E-03	1.7E-02	7.1E-02	9.4E-02	1.1E-01	1.6E-01	2.2E-01	2.9E-01	3.4E-01
NH_3	2.6E-05	3.2E-05	4.0E-05	5.1E-05	6.7E-05	8.8E-05	1.2E-04	1.6E-04	2.3E-04	2.6E-04	3.0E-04	3.7E-04	4.4E-04	4.9E-04	5.0E-04
Total P (bar)	139.8	139.8	139.8	139.8	139.8	139.8	139.8	139.8	139.8	133.2	125.3	110.9	100.5	93.8	89.9
Condensed phases															
Graphite (moles)										0.23067	0.503	0.9996	1.3633	1.5928	1.7252
Graphite (mass)										2.7705	6.0413	12.006	16.374	19.13	20.721
Water (moles)															
Water (mass)															

Table S8-III. Fugacities (bar), in moles, of species in a real gas calculated according to FactSage simulating closed system cooling of a magma ocean at ΔIW+0.5 from 2173 K to 273 K with initial molar ratios of H/C = 0.22 and H/N = 5.8. Part III – 723 K – 273 K.

Temp. (K)	723	673	623	573	523	473	423	373	323	273
Gas (moles)	3.0611	3.0216	3.0015	2.9919	2.9876	2.9858	2.9852	2.985	2.8282	2.5
CO	1.9	0.6	0.2	0.0	0.0	0.0	0.0	0.0	0.0	0.0
CO_2	69.4	69.5	69.4	69.2	69.1	69.0	68.9	68.8	68.8	68.8
H_2O	11.2	12.1	12.9	13.3	13.7	13.9	14.1	14.2	9.8	0.4
H_2	2.4	1.4	0.8	0.4	0.1	0.0	0.0	0.0	0.0	0.0
N_2	2.4	2.4	2.4	2.4	2.4	2.4	2.4	2.4	2.4	2.4
O_2	2.1E-29	1.6E-31	5.8E-34	7.6E-37	2.8E-40	2.0E-44	1.4E-49	4.4E-56	1.4E-64	<1.0E-70
O	6.5E-30	2.6E-32	4.1E-35	2.2E-38	2.7E-42	5.2E-47	7.6E-53	3.1E-60	6.7E-70	<1.0E-70
CH_4	3.7E-01	3.8E-01	3.6E-01	3.1E-01	2.6E-01	1.9E-01	1.3E-01	7.7E-02	1.8E-02	1.2E-05
NH_3	4.8E-04	4.2E-04	3.4E-04	2.6E-04	1.8E-04	1.1E-04	6.0E-05	2.7E-05	5.5E-06	1.2E-08
Total P (bar)	87.7	86.5	86.0	85.7	85.6	85.6	85.5	85.5	81.0	71.6
Condensed phases										
Graphite (moles)	1.7979	1.8369	1.8584	1.8711	1.8796	1.8858	1.8907	1.8946	1.8988	1.9
Graphite (mass)	21.594	22.063	22.321	22.474	22.575	22.65	22.709	22.755	22.805	22.82
Water (moles)									0.1568	0.48505
Water (mass)									2.8247	8.7383

Effect of H/C ratio and log fO_2 on atmosphere speciation

Due to the uncertainty of the solubility of H and C in peridotite liquids, we explore the effect of the H/C ratio of the atmosphere on the stability of C- and H-bearing species at both high (2173 K) and low (300 K) temperatures. Here, we keep the molar quantities of C (4.3) and N (0.17) constant, and modify the number of moles of H from 0.05 to 61.85, in order to produce molar log(H/C) ratios between -0.73 and 1.16 (the BSE ratio of ref. (*24*)). The moles of O are modified in order to bracket the appropriate values relative to IW at 2173 K, between ΔIW-2.5 and ΔIW+2.5. For this exercise the total pressure is kept constant at 100 bar. In order to populate the parameter space densely enough to interpolate between individual point calculations, 21,000 Gibbs free energy minimisations were performed at both 300 K and 2173 K, and interpolated linearly to produce Fig. 4. An output of the calculation is available from the corresponding author upon request.

To explore how fO_2 evolves upon cooling, calculations were performed from 2173 K to 300 K at 50 K intervals, each starting with a fixed ΔIW (-1.25), with log(H/C) varying from -0.73 to 1.05 (Fig. S10) at 100 bar. Similar trends are observed for different starting fO_2, shifted to lower H/C (lower fO_2), and vice-versa. Graphite saturation is reached at progressively lower temperatures at increasing H/C ('C in' line in Fig. S10), and does not occur for log(H/C) > 0.8. Graphite precipitation increases the ΔIW of the atmosphere through the reaction $CO(g) = C(s) + ½O_2(g)$. For high H/C atmospheres, the lack of graphite precipitation keeps the ΔIW relatively constant, until the condensation of liquid water. This occurs relatively isothermally (within the uncertainty of ±50 K calculaton steps) across all H/C ratios. Depending on the pre-existing composition of the atmosphere, H_2O condensation produces an increase (log(H/C) < 0.4)), a mild- to moderate decrease (0.4 < log(H/C) < 0.8) or a strong decrease for log(H/C) > 0.8. This occurs because, even though the reaction itself is independent of fO_2, H_2O (g) = H_2O (l), H is extracted at a constant molar ratio relative to O of 2:1, whereas the atmosphere contains a finite quantity of these two components. As such, removal of the minor amount of the abundant H present in a high H/C atmosphere, compared to the limited O budget of the atmosphere, has the effect of reducing O_2 even further (*i.e.,* the mole fraction of O decreases at the expense of H). The situation is reversed for a low H/C atmosphere, where the removal of H increases the relative proportion of O in the atmosphere (XO increases whereas XH decreases), thus increasing ΔIW.

The above discussion highlights the causes for the observed distribution of atmospheric species as a function of ΔIW and log(H/C) displayed in Fig. 4.

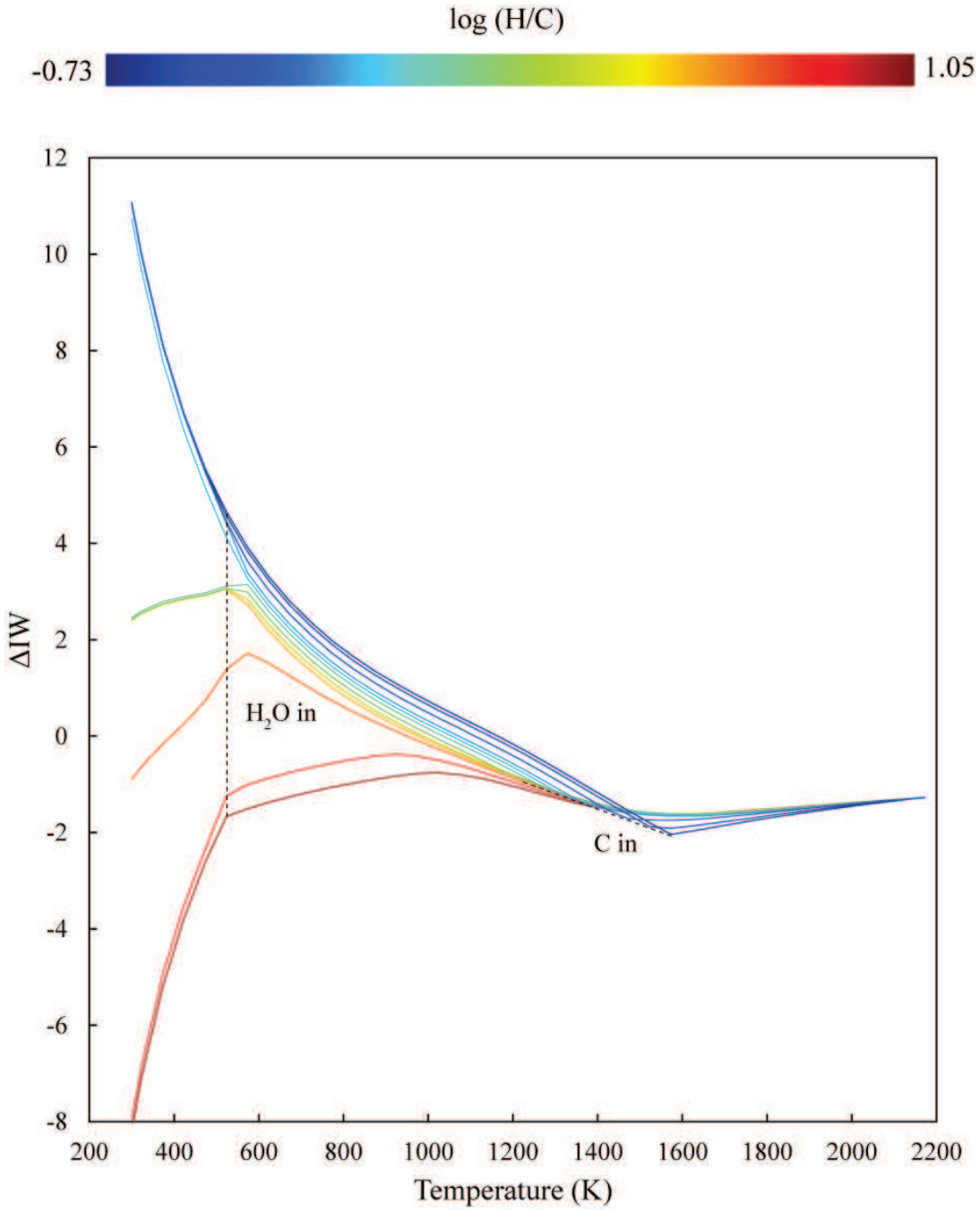

Fig. S10. Relative oxygen fugacity as a function of temperature in a cooling magma ocean-generated atmosphere with variable H/C. Isochemical cooling calculations showing the variation of fO_2 (relative to the Iron-Wüstite buffer, ΔIW) as a function of absolute temperature (K). Lines are colour-coded according to the log(H/C) of the starting gas, which all have a common fO_2 of ΔIW-1.25 at 2173 K. Graphite precipitation ('C in') and liquid water condensation ('H_2O in') are demarcated by dashed black lines.

REFERENCES AND NOTES

1. D. M. Hunten, Atmospheric evolution of the terrestrial planets. *Science* **259**, 915–920 (1993).
2. H. Lammer, A. L. Zerkle, S. Gebauer, N. Tosi, L. Noack, M. Scherf, E. Pilat-Lohinger, M. Güdel, J. L. Grenfell, M. Godolt, A. Nikolaou, Origin and evolution of the atmospheres of early Venus, Earth and Mars. *Astron. Astrophys. Rev.* **26**, 2 (2018).
3. A. Morbidelli, J. I. Lunine, D. P. O'Brien, S. N. Raymond, K. J. Walsh, Building terrestrial planets. *Annu. Rev. Earth Planet. Sci.* **40**, 251–275 (2012).
4. B. Marty, The origins and concentrations of water, carbon, nitrogen and noble gases on Earth. *Earth Planet. Sci. Lett.* **313**–**314**, 56–66 (2012).
5. F. Albarède, Volatile accretion history of the terrestrial planets and dynamic implications. *Nature* **461**, 1227–1233 (2009).
6. H. J. Melosh, Giant impacts and the thermal state of the early Earth, in *Origin of the Earth,* H. E. Newsom, J. H. Jones, Eds. (Oxford Univ., New York, 1990), pp. 69–83.
7. H. Genda, Y. Abe, Modification of a proto-lunar disk by hydrodynamic escape of silicate vapor. *Earth Planets Sp.* **53**, 53–57 (2003).
8. M. M. Hirschmann, Magma ocean influence on early atmosphere mass and composition. *Earth Planet. Sci. Lett.* **341**–**344**, 48–57 (2012).
9. K. Zahnle, L. Schaefer, B. Fegley, Earth's earliest atmospheres. *Cold Spring Harb. Perspect. Biol.* **2**, a004895 (2010).
10. F. W. Aston, The rarity of the inert gases on the Earth. *Nature* **114**, 786 (1924).
11. H. Brown, Rare gases and the formation of Earth's atmosphere, in *The Atmosphere of the Earth and Planets,* G. Kuiper, Ed. (University of Chicago Press, Chicago, 1949), pp. 258–266.
12. J. H. J. Poole, The evolution of the earth's atmosphere. *Sci. Proc. R. Dublin Soc.* **25**, 201–224 (1951).
13. H. D. Holland, Model for the evolution of the Earth's atmosphere, in *Petrologic Studies: A Volume in Honor of A.F. Buddington,* E. J. Engle, H. L. James, B. F. Leonard, Eds. (Geological Society of America, 1962), pp. 447–477.
14. R. E. Lupu, K. Zahnle, M. S. Marley, L. Schaefer, B. Fegley, C. Morley, K. Cahoy, R. Freedman, J. J. Fortney, The atmospheres of Earth-like planets after giant impact events. *Astrophys. J.* **784**, 1–19 (2014).
15. F. Tian, O. B. Toon, A. A. Pavlov, H. De Sterck, A hydrogen-rich early Earth atmosphere. *Science* **308**, 1014–1017 (2005).
16. H. C. Urey, On the early chemical history of the Earth and the origin of life. *Proc. Natl. Acad. Sci. U.S.A.* **38**, 351–363 (1952).
17. K. J. Zahnle, R. Lupu, D. C. Catling, N. Wogan, Creation and evolution of impact-generated reduced atmospheres of early Earth. *Planet. Sci. J.* **1**, 1–21 (2020).
18. S. L. Miller, A production of amino acids under possible primitive earth conditions. *Science* **117**, 528–529 (1953).
19. L. Schaefer, B. Fegley Jr., Redox states of initial atmospheres outgassed on rocky planets and planetesimals. *Astrophys. J.* **843**, 120 (2017).
20. Z. D. Sharp, Nebular ingassing as a source of volatiles to the terrestrial planets. *Chem. Geol.* **448**, 137–150 (2017).
21. J. F. Kasting, Earth's early atmosphere. *Science* **259**, 920–926 (1993).
22. V. Stagno, Carbon, carbides, carbonates and carbonatitic melts in the Earth's interior. *J. Geol. Soc. Lond.* **176**, 375–387 (2019).

23. D. J. Frost, U. Mann, Y. Asahara, D. C. Rubie, The redox state of the mantle during and just after core formation. *Philos. Trans. A. Math. Phys. Eng. Sci.* **366**, 4315–4337 (2008).
24. H. Palme, H. St. C. O'Neill, Cosmochemical estimates of mantle composition, in *Treatise on Geochemistry, Vol. 3: The Mantle and Core*, R. W. Carlson, Ed. (Elsevier B.V., ed. 2, 2014), pp. 1–39.
25. A. B. Woodland, J. Kornprobst, B. J. Wood, Oxygen thermobarometry of orogenic lherzolite massifs. *J. Petrol.* **33**, 203–230 (1992).
26. A. B. Woodland, M. Koch, Variation in oxygen fugacity with depth in the upper mantle beneath the Kaapvaal craton, Southern Africa. *Earth Planet. Sci. Lett.* **214**, 295–310 (2003).
27. V. Stagno, D. O. Ojwang, C. A. McCammon, D. J. Frost, The oxidation state of the mantle and the extraction of carbon from Earth's interior. *Nature* **493**, 84–88 (2013).
28. H. St. C. O'Neill, D. C. Rubie, D. Canil, C. A. Geiger, C. R. Ross II, F. Seifert, A. B. Woodland, Ferric iron in the upper mantle and in transition zone assemblages: Implications for relative oxygen fugacities in the mantle, in *Evolution of the Earth and Planets*, E. Takahashi, R. Jeanloz, D. C. Rubie, Eds. (American Geophysical Union, 1993), pp. 73–88.
29. V. C. Kress, I. S. E. Carmichael, The compressibility of silicate liquids containing Fe_2O_3 and the effect of composition, temperature, oxygen fugacity and pressure on their redox states. *Contrib. Mineral. Petrol.* **108**, 82–92 (1991).
30. E. Cottrell, K. A. Kelley, The oxidation state of Fe in MORB glasses and the oxygen fugacity of the upper mantle. *Earth Planet. Sci. Lett.* **305**, 270–282 (2011).
31. A. J. Berry, G. A. Stewart, H. St. C. O'Neill, G. Mallmann, J. F. W. Mosselmans, A re-assessment of the oxidation state of iron in MORB glasses. *Earth Planet. Sci. Lett.* **483**, 114–123 (2018).
32. H. Wänke, G. Dreibus, Chemical composition and accretion history of terrestrial planets. *Philos. Trans. R. Soc. Lond.* **325**, 545–557 (1988).
33. A. E. Ringwood, Chemical evolution of the terrestrial planets. *Geochim. Cosmochim. Acta* **30**, 41–104 (1966).
34. E. Takahashi, Melting of a dry peridotite KLB-1 up to 14 GPa: Implications on the origin of peridotitic upper mantle. *J. Geophys. Res.* **91**, 9367–9382 (1986).
35. M. J. Walter, Melting of garnet peridotite and the origin of komatiite and depleted lithosphere. *J. Petrol.* **39**, 29–60 (1998).
36. G. S. Nikolaev, A. A. Borisov, A. A. Ariskin, Calculation of the ferric–ferrous ratio in magmatic melts: Testing and additional calibration of empirical equations for various magmatic series. **34**, 641–649 (1996).
37. A. Borisov, H. Behrens, F. Holtz, Ferric/ferrous ratio in silicate melts: A new model for 1 atm data with special emphasis on the effects of melt composition. *Contrib. Mineral. Petrol.* **173**, 98 (2018).
38. K. D. Jayasuriya, H. St. C. O'Neill, A. J. Berry, S. J. Campbell, A Mössbauer study of the oxidation state of Fe in silicate melts. *Am. Mineral.* **89**, 1597–1609 (2004).
39. H. St. C. O'Neill, A. J. Berry, G. Mallmann, The oxidation state of iron in mid-ocean ridge basaltic (MORB) glasses: Implications for their petrogenesis and oxygen fugacities. *Earth Planet. Sci. Lett.* **504**, 152–162 (2018).
40. D. Canil, H. St. C. O'Neill, D. G. Pearson, R. L. Rudnick, W. F. McDonough, D. A. Carswell, Ferric iron in peridotites and mantle oxidation states. *Earth Planet. Sci. Lett.* **123**, 205–220 (1994).
41. A. B. Woodland, J. Kornprobst, A. Tabit, Ferric iron in orogenic lherzolite massifs and controls of oxygen fugacity in the upper mantle. *Lithos* **89**, 222–241 (2006).

42. P. A. Sossi, S. Klemme, H. St. C. O'Neill, J. Berndt, F. Moynier, Evaporation of moderately volatile elements from silicate melts: Experiments and theory. *Geochim. Cosmochim. Acta* **260**, 204–231 (2019).
43. M. W. Chase, NIST-JANAF Thermochemical Tables, 4th Ed., in *Monograph 9 (Part I and Part II)* (Journal of Physical and Chememical Reference Data Monographs, ed. 4, 1998).
44. V. Solomatov, Magma oceans and primordial mantle differentiation, in *Treatise of Geophysics Second Edition*, G. Schubert, Ed. (Elsevier B.V., ed. 2, 2015), pp. 81–104.
45. A. Nikolaou, N. Katyal, N. Tosi, M. Godolt, J. L. Greenfell, H. Rauer, What factors affect the duration and outgassing of the terrestrial magma ocean? *Astrophys. J.* **875**, 11 (2019).
46. D. J. Bower, D. Kitzmann, A. S. Wolf, P. Sanan, C. Dorn, A. V. Oza, Linking the evolution of terrestrial interiors and an early outgassed atmosphere to astrophysical observations. *Astron. Astrophys.* **631**, A103 (2019).
47. S. Aulbach, V. Stagno, Evidence for a reducing Archean ambient mantle and its effects on the carbon cycle. *Geology* **44**, 751–754 (2016).
48. R. W. Nicklas, I. S. Puchtel, R. D. Ash, P. M. Piccoli, E. Hanski, E. Nisbet, P. Waterton, D. G. Pearson, A. D. Anbar, Secular mantle oxidation across the Archean-Proterozoic boundary: Evidence from V partitioning in komatiites and picrites. *Geochim. Cosmochim. Acta* **250**, 49–75 (2019).
49. J. W. Delano, Redox history of the Earth's interior since ~3900 Ma: Implications for prebiotic molecules. *Orig. Life Evol. Biosph.* **31**, 311–341 (2001).
50. D. Trail, E. B. Watson, N. D. Tailby, The oxidation state of Hadean magmas and implications for early Earth's atmosphere. *Nature* **480**, 79–82 (2011).
51. A. Bézos, E. Humler, The $Fe^{3+}/\Sigma Fe$ ratios of MORB glasses and their implications for mantle melting. *Geochim. Cosmochim. Acta* **69**, 711–725 (2005).
52. K. Armstrong, D. J. Frost, C. A. McCammon, D. C. Rubie, T. Boffa Ballaran, Deep magma ocean formation set the oxidation state of Earth's mantle. *Science* **365**, 903–906 (2019).
53. M. M. Hirschmann, Comparative deep Earth volatile cycles: The case for C recycling from exosphere/mantle fractionation of major (H_2O, C, N) volatiles and from H_2O/Ce, CO_2/Ba, and CO_2/Nb exosphere ratios. *Earth Planet. Sci. Lett.* **502**, 262–273 (2018).
54. G. Moore, T. Vennemann, I. S. E. Carmichael, An empirical model for the solubility of H_2O in magmas to 3 kilobars. *Am. Mineral.* **83**, 36–42 (1998).
55. J. E. Dixon, E. M. Stolper, J. R. Holloway, An experimental study of water and carbon dioxide solubilities in mid-ocean ridge basaltic liquids. Part I: Calibrations and solubility models. *J. Petrol.* **36**, 1607–1631 (1995).
56. G. Libourel, B. Marty, F. Humbert, Nitrogen solubility in basaltic melt. Part I. Effect of oxygen fugacity. *Geochim. Cosmochim. Acta* **67**, 4123–4135 (2003).
57. D. T. Wetzel, M. J. Rutherford, S. D. Jacobsen, E. H. Hauri, A. E. Saal, Degassing of reduced carbon from planetary basalts. *Proc. Natl. Acad. Sci. U.S.A.* **110**, 8010–8013 (2013).
58. E. Stolper, Water in silicate glasses: An infrared spectroscopic study. *Contrib. Mineral. Petrol.* **81**, 1–17 (1982).
59. D. S. Grewal, R. Dasgupta, C. Sun, K. Tsuno, G. Costin, Delivery of carbon, nitrogen, and sulfur to the silicate Earth by a giant impact. *Sci. Adv.* **5**, eaau3669 (2019).
60. T. Yoshioka, D. Nakashima, T. Nakamura, S. Shcheka, H. Keppler, Carbon solubility in silicate melts in equilibrium with a CO-CO_2 gas phase and graphite. *Geochim. Cosmochim. Acta* **259**, 129–143 (2019).

61. C. W. Bale, E. Bélisle, P. Chartrand, S. A. Decterov, G. Eriksson, A. E. Gheribi, K. Hack, I.-H. Jung, Y.-B. Kang, J. Melançon, A. D. Pelton, S. Petersen, C. Robelin, J. Sangster, P. Spencer, M.-A. Van Ende, FactSage thermochemical software and databases, 2010-2016. *Calphad* **55**, 1–19 (2016).
62. H. Keppler, G. Golabek, Graphite floatation on a magma ocean and the fate of carbon during core formation. *Geochem. Perspect. Lett.* **11**, 12–17 (2019).
63. A. Toramaru, N. Fujii, Connectivity of melt phase in a partially molten peridotite. *J. Geophys. Res.* **91**, 9239–9252 (1986).
64. L. T. Elkins-Tanton, Linked magma ocean solidification and atmospheric growth for Earth and Mars. *Earth Planet. Sci. Lett.* **271**, 181–191 (2008).
65. S. Hier-Majumder, M. M. Hirschmann, The origin of volatiles in the Earth's mantle. *Geochem. Geophys. Geosyst.* **18**, 3078–3092 (2017).
66. Q. Bai, D. L. Kohlstedt, Substantial hydrogen solubility in olivine and implications for water storage in the mantle. *Nature* **357**, 672–674 (1992).
67. K. J. Zahnle, M. S. Marley, Methane, carbon monoxide, and ammonia in brown dwarfs and self-luminous giant planets. *Astrophys. J.* **797**, 41 (2014).
68. A. C. Lasaga, H. D. Holland, M. J. Dwyer, Primordial oil slick. *Science* **174**, 53–55 (1971).
69. L. Schaefer, K. Lodders, B. Fegley, Vaporization of the earth: Application to exoplanet atmospheres. *Astrophys. J.* **755**, 41 (2012).
70. M. Fischer-Gödde, B.-M. Elfers, C. Münker, K. Szilas, W. D. Maier, N. Messling, T. Morishita, M. van Kranendonk, H. Smithies, Ruthenium isotope vestige of Earth's pre-late-veneer mantle preserved in Archaean rocks. *Nature* **579**, 240–244 (2020).
71. G. Mallmann, H. St. C. O'Neill, The crystal/melt partitioning of V during mantle melting as a function of oxygen fugacity compared with some other elements (Al, P, Ca, Sc, Ti, Cr, Fe, Ga, Y, Zr and Nb). *J. Petrol.* **50**, 1765–1794 (2009).
72. G. Dreibus, H. Wanke, Volatiles on Earth and Mars: A comparison. *Icarus* **71**, 225–240 (1987).
73. D. P. O'Brien, A. Izidoro, S. A. Jacobson, S. N. Raymond, D. C. Rubie, The delivery of water during terrestrial planet formation. *Space Sci. Rev.* **214**, 47 (2018).
74. J. F. Kasting, Runaway and moist greenhouse atmospheres and the evolution of Earth and Venus. *Icarus* **74**, 472–494 (1988).
75. M. H. Carr, Mars: A water-rich planet? *Icarus* **68**, 187–216 (1986).
76. L. H. Kellogg, H. Lokavarapu, D. L. Turcotte, Carbonation and the Urey reaction. *Am. Mineral.* **104**, 1365–1368 (2019).
77. L.-g. Liu, The inception of the oceans and CO_2-atmosphere in the early history of the Earth. **227**, 179–184 (2004).
78. N. H. Sleep, K. Zahnle, P. S. Neuhoff, Initiation of clement surface conditions on the earliest Earth. *Proc. Natl. Acad. Sci. U.S.A.* **98**, 3666–3672 (2001).
79. F. Nimmo, D. McKenzie, Volcanism and tectonics on Venus. *Annu. Rev. Earth Planet. Sci.* **26**, 23–51 (1998).
80. P. Van Thienen, N. J. Vlaar, A. P. Van Den Berg, Plate tectonics on the terrestrial planets. *Phys. Earth Planet. Inter.* **142**, 61–74 (2004).
81. H. J. Cleaves, J. H. Chalmers, A. Lazcano, S. L. Miller, J. L. Bada, A reassessment of prebiotic organic synthesis in neutral planetary atmospheres. *Orig. Life Evol. Biosph.* **38**, 105–115 (2008).
82. A.-L. Auzende, J. Gillot, A. Coquet, L. Hennet, G. Ona-Nguema, D. Bonnin, I. Esteve, M. Roskosz, G. Fiquet, Synthesis of amorphous MgO-rich peridotitic starting material for laser-heated diamond anvil cell experiments – application to iron partitioning in the mantle. *High Press. Res.* **31**, 199–213 (2011).

83. W. E. Jackson, F. Farges, M. Yeager, P. A. Mabrouk, S. Rossano, G. A. Waychunas, E. I. Solomon, G. E. Brown Jr., Multi-spectroscopic study of Fe(II) in silicate glasses: Implications for the coordination environment of Fe(II) in silicate melts. *Geochim. Cosmochim. Acta* **69**, 4315–4332 (2005).
84. S. Bajt, S. R. Sutton, J. S. Delaney, X-ray microprobe analysis of iron oxidation states in silicates and oxides using x-ray absorption near edge structure (XANES). *Geochim. Cosmochim. Acta* **58**, 5209–5214 (1994).
85. J. E. Mungall, Empirical models relating viscosity and tracer diffusion in magmatic silicate melts. *Geochim. Cosmochim. Acta* **66**, 125–143 (2002).
86. Y. Zhang, H. Ni, Y. Chen, Diffusion data in silicate melts. *Rev. Mineral. Geochem*. **72**, 311–408 (2010).
87. H. St. C. O'Neill, S. M. Eggins, The effect of melt composition on trace element partitioning: An experimental investigation of the activity coefficients of FeO, NiO, CoO, MoO_2 and MoO_3 in silicate melts. *Chem. Geol.* **186**, 151–181 (2002).
88. V. P. Glushko, V. A. Medvedev, L. V. Gurvich, V. S. Yungman, *Thermal Constants of Substances* (John Wiley & Sons, ed. 1, 1999).
89. W. F. McDonough, S.-s. Sun, The composition of the Earth. *Chem. Geol.* **120**, 223–253 (1995).
90. D. Canil, H. St. C. O'Neill, Distribution of ferric iron in some upper-mantle assemblages. *J. Petrol.* **37**, 609–635 (1996).
91. F. R. Boyd, D. G. Pearson, P. H. Nixon, S. A. Mertzman, Low-calcium garnet harzburgites from southern Africa: Their relations to craton structure and diamond crystallization. *Contrib. Mineral. Petrol.* **113**, 352–366 (1993).
92. F. A. Frey, D. H. Green, The mineralogy, geochemistry and origin of Iherzolite inclusions in Victorian basanites. *Geochem. Cosmochim. Acta* **38**, 1023–1059 (1974).
93. L. E. Wasylenki, M. B. Baker, A. J. R. Kent, E. M. Stolper, Near-solidus melting of the shallow upper mantle: Partial melting experiments on depleted peridotite. *J. Petrol.* **44**, 1163–1191 (2003).
94. M. J. Walter, Melt extraction and compositional variability in mantle lithosphere, in *Treatise on Geochemistry*, R. W. Carlson, Ed. (Elsevier, 2003), vol. 2, pp. 363–394.
95. R. K. Workman, S. R. Hart, Major and trace element composition of the depleted MORB mantle (DMM). *Earth Planet. Sci. Lett.* **231**, 53–72 (2005).
96. Z. Wang, H. Becker, Ratios of S, Se and Te in the silicate Earth require a volatile-rich late veneer. *Nature* **499**, 328–331 (2013).
97. M. M. Hirschmann, A. C. Withers, P. Ardia, N. T. Foley, Solubility of molecular hydrogen in silicate melts and consequences for volatile evolution of terrestrial planets. *Earth Planet. Sci. Lett.* **345**–**348**, 38–48 (2012).
98. E. Stolper, J. R. Holloway, Experimental determination of the solubility of carbon dioxide in molten basalt at low pressure. *Earth Planet. Sci. Lett.* **87**, 397–408 (1988).
99. D. L. Hamilton, S. Oxtoby, Solubility of water in albite-melt determined by the weight-loss method. *J. Geol.* **94**, 626–630 (1986).
100. V. Pan, J. R. Holloway, R. L. Hervig, The pressure and temperature dependence of carbon dioxide solubility in tholeiitic basalt melts. *Geochim. Cosmochim. Acta* **55**, 1587–1595 (1991).